nature genetics

Article

https://doi.org/10.1038/s41588-024-01874-9

In vivo CRISPR screens identify a dual function of MEN1 in regulating tumor–microenvironment interactions

Received: 10 November 2023

Accepted: 18 July 2024

Peiran Su[1,2,13], Yin Liu[3,13], Tianyi Chen[2,13], Yibo Xue[2], Yong Zeng[2], Guanghui Zhu[2,12], Sujun Chen[2,12], Mona Teng[1,2], Xinpei Ci[2], Mengdi Guo[2,4], Michael Y. He[2], Jun Hao[2], Vivian Chu[1,2], Wenxi Xu[2], Shiyan Wang[2,5], Parinaz Mehdipour[6], Xin Xu[2], Sajid A. Marhon[2], Fraser Soares[2], Nhu-An Pham[2], Bell Xi Wu[1,2], Peter Hyunwuk Her[1,2], Shengrui Feng[1,2], Najd Alshamlan[2], Maryam Khalil[2,7], Rehna Krishnan[2], Fangyou Yu[3], Chang Chen[8], Francis Burrows[9], Razqallah Hakem[1,2], Mathieu Lupien[1,2], Shane Harding[1,2], Benjamin H. Lok[1,2], Catherine O'Brien[1,2], Alejandro Berlin[2], Daniel D. De Carvalho[1,2], David G. Brooks[2,4], Daniel Schramek[10,11], Ming-Sound Tsao[1,2,7] ✉ & Housheng Hansen He[1,2] ✉

Functional genomic screens in two-dimensional cell culture models are limited in identifying therapeutic targets that influence the tumor microenvironment. By comparing targeted CRISPR–Cas9 screens in a two-dimensional culture with xenografts derived from the same cell line, we identified *MEN1* as the top hit that confers differential dropout effects in vitro and in vivo. *MEN1* knockout in multiple solid cancer types does not impact cell proliferation in vitro but significantly promotes or inhibits tumor growth in immunodeficient or immunocompetent mice, respectively. Mechanistically, MEN1 knockout redistributes MLL1 chromatin occupancy, increasing H3K4me3 at repetitive genomic regions, activating double-stranded RNA expression and increasing neutrophil and CD8$^+$ T cell infiltration in immunodeficient and immunocompetent mice, respectively. Pharmacological inhibition of the menin–MLL interaction reduces tumor growth in a CD8$^+$ T cell-dependent manner. These findings reveal tumor microenvironment-dependent oncogenic and tumor-suppressive functions of *MEN1* and provide a rationale for targeting *MEN1* in solid cancers.

Tumor masses are mixtures of cancerous and normal cells that collectively form the tumor microenvironment (TME)[1]. Within the TME, various cell populations communicate through cytokines, chemokines and growth factors, further recruiting additional infiltrating cells, leading to increased tumor heterogeneity[2–4]. Advances in single-cell RNA sequencing (scRNA-seq) technology allow for the characterization of individual components within the TME, offering significant opportunities to enhance our understanding of tumor biology and cancer management[5,6]. Indeed, in recent years, an increasing number of studies has focused on targeting components of the TME, particularly the immune microenvironment[7,8].

The CRISPR screen is a powerful tool to identify vulnerabilities in cancer cells[9,10]. Although CRISPR screens have been extensively conducted in in vitro cell culture systems[11–13], including the Cancer Dependency Map (DepMap) project[14–16], the absence of the TME in these models has limited the ability to identify gene targets that modulate

A full list of affiliations appears at the end of the paper. ✉e-mail: Ming.Tsao@uhn.ca; hansenhe@uhnresearch.ca

interactions between tumor and the TME. A few recent studies of in vivo CRISPR screens have identified targets that regulate immunotherapy resistance, highlighting the feasibility and significance of functional genomic screens in the context of physiologic TME[12,17,18].

In this study, we set out to identify modulators of the tumor–TME interactions. By directly comparing parallel in vitro and in vivo CRISPR screens, we identified *MEN1* as the top candidate gene that confers differential effects in cell culture versus xenograft tumors. We found that *MEN1* knockout resulted in increased tumor growth in immunodeficient mice but decreased growth in immunocompetent mice, revealing both TME-dependent oncogenic and tumor-suppressive functions. Our findings underscore the effectiveness of in vivo functional genomic screens in identifying clinically relevant drug targets and provide a rationale for the therapeutic targeting of *MEN1*, either alone or in combination with immunotherapy, in multiple solid and hematologic cancer types.

Results

Parallel in vitro and in vivo CRISPR screens in lung cancer

The number of cells that can be injected in mice to form xenograft tumors is limited. Therefore, we designed a targeted single guide RNA (sgRNA) library to ensure sufficient coverage of each sgRNAs in an in vivo screen. This library, referred to as Epi-Drug[19,20], comprises 12,472 sgRNAs targeting 317 epigenetic regulators and 657 DrugBank targets, with an average of 10 sgRNAs per gene (Extended Data Fig. 1a and Supplementary Table 1). A549 lung adenocarcinoma (LUAD) cells with stable Cas9 expression were transduced with the sgRNA library and cultured in Petri dishes for 3 days with puromycin selection (D0). Subsequently, the transduced cells were split into equal aliquots for either Petri dish culture or establishing xenograft tumors via subcutaneous injection into immunodeficient NOD scid gamma (NSG) mice (Fig. 1a). Two-dimensional (2D) cultured cells and xenograft tumors were collected at day 21 (D21) for DNA extraction and next-generation sequencing (NGS).

We observed high overall sgRNA coverages, with 99.98% and 97.49% of the 12,472 sgRNAs detected in D21 cultured cells and xenograft tumors, respectively (Extended Data Fig. 1b). Xenograft tumors demonstrated greater variation in sgRNA representation compared with cultured cells (Extended Data Fig. 1c,d), consistent with a previous report[21]. In both the in vitro and in vivo screens, MAGeCK[22] analysis revealed significantly higher dropout rates for the positive control genes (Mann–Whitney U-test; $P = 2.10 \times 10^{-21}$), compared with negative controls (Extended Data Fig. 1e,f), suggesting the high efficacy of the screens.

We then applied MAGeCK to identify genes with sgRNAs that were depleted or enriched in D21 compared with D0 (referred to as dropout and enriched genes hereafter). This led to the identification of 47 and 72 dropout genes in the in vitro and in vivo screens, respectively (Extended Data Fig. 1g,h and Supplementary Table 2). Twenty-two dropout genes were found to be common to both screens (Supplementary Table 2), including DepMap core essential genes *POLE* and *POLE2* (ref. 23). Although no significantly enriched genes were found in vitro, 40 were found in the in vivo screens (Extended Data Fig. 1g,h and Supplementary Table 2). To further identify genes that confer differential essentialities in vitro and in vivo, we used MAGeCK to compare the D21 cell culture and xenograft tumor screens directly. This analysis identified 12 in vivo specific dropout genes and 13 enriched genes (Fig. 1b and Supplementary Table 2). Among these genes, the top hit, *MEN1*, which encodes menin, is of particular interest. Genetic loss of *MEN1* drives tumorigenesis in multiple solid cancer types. However, the dependency score of *MEN1* from DepMap showed that it is not an enriched gene in in vitro screens for 953 of 954 cell lines from solid tumor types (Extended Data Fig. 1i). The in vivo specific enrichment in A549 suggests that *MEN1* may function through regulating tumor–TME interactions.

MEN1 regulates cytokine genes both in vitro and in vivo

To validate our findings, we designed two sgRNAs for *MEN1* deletion (Extended Data Fig. 2a). Tumor growth significantly increased with both MEN1 knockout sgRNAs (Fig. 1c). By contrast, no obvious effect on colony formation or cell proliferation was observed in 2D cultures upon genetic ablation of MEN1 (Fig. 1d and Extended Data Fig. 2b). These data further confirm the in vivo restricted function of MEN1 in this context.

To investigate the mechanisms underlying the function of MEN1, we conducted RNA sequencing (RNA-seq) in 2D cultured A549 cells with and without MEN1 knockout. Differential gene analysis using DESeq2 (ref. 24) identified 357 upregulated and 252 downregulated genes on *MEN1* knockout ($P_{\mathrm{adj}} \leq 0.01$ and $\mathrm{abs}(\log_2(\text{fold change})) > 1$; Extended Data Fig. 2c). Kyoto Encyclopedia of Genes and Genomes (KEGG) pathway analysis revealed 'cytokine–cytokine receptor interaction' as the most significantly enriched pathway in the upregulated genes (Fig. 1e, Extended Data Fig. 2d and Supplementary Table 3). Although a smaller number of differential genes were identified in xenograft tumors (Extended Data Fig. 2e), likely because of the heterogeneity of tumor samples, 'cytokine–cytokine receptor interaction' remained the top enriched pathway in the upregulated genes (Fig. 1f and Supplementary Table 3). Quantitative real-time polymerase chain reaction with reverse transcription (RT–qPCR) analysis of representative genes in the 'cytokine–cytokine receptor interaction' signature, including *CXCL1*, *IL33*, *CXCL8* and *IL1B*, showed marked upregulation upon *MEN1* depletion in A549 and NCI-H1792, an additional human LUAD cell line (Fig. 1g and Extended Data Fig. 2f,g). Notably, through reanalysis of five RNA-seq datasets from recent publications on MEN1 functions[25–29], we consistently observed cytokine-related signatures as top enriched terms in response to MEN1 perturbation in four of the datasets, utilizing both cancer cell line and patient-derived xenograft (PDX) models (Extended Data Fig. 3a–d).

Fig. 1 | Parallel in vivo and in vitro CRISPR screens in A549 and in vivo specific function of MEN1 in lung cancer. a, Schematic representation of the CRISPR screen experiment design. A549 cells with stable Cas9 expression were transduced with Epi-Drug sgRNA library and selected with puromycin for 3 days (D0). Parallel in vitro and in vivo screens were performed for 3 weeks (D21). Samples were collected for PCR amplification and NGS. **b**, Dropout (genes with sgRNA reduced in D21; blue dots) and enriched (genes with sgRNA increased in D21; red dots) genes in LUAD A549 xenograft compared with A549 2D cultured cells. The P values of positive and negative selections and $\log_2$(fold change) were defined and calculated using MAGeCK. *MEN1* is the top ranked enriched gene. **c**, Xenograft tumor growth curve in immunodeficient mice inoculated with control (sgCtrl) or MEN1 knockout (sgMEN1-1, sgMEN1-2) A549 cells. Each data point represents mean ± s.e.m. tumor volumes ($n = 5$ in sgCtrl, sgMEN1-1 and sgMEN1-2 groups). Two-way ANOVA was used for the growth curves. $^*P < 0.05$, $^{**}P < 0.01$. **d**, Colony formation of A549 cells with (sgMEN1) and without (sgCtrl) knockout of MEN1. Cells were seeded in six-well plates in duplicate and allowed to grow for 8 days before staining with crystal violet. Scale bars, 7 mm. **e**,**f**, KEGG analysis of differential genes in MEN1 knockout versus control A549 cells in vitro (**e**) and in vivo (**f**). The x axis represents the number of genes. Wald tests defined in DEseq2 were used to calculate P values. **g**, RT–qPCR showing the expression of representative cytokine-related genes in MEN1 knockout A549 cells relative to control. Housekeeping gene TBP was used as a control. Mean ± s.e.m. of three biological replicates is shown (unpaired two-tailed Student's t-test). **h**, KEGG analysis of differential genes in MEN1-low versus MEN1-high patients from the TCGA LUAD cohort. Wald tests defined in DEseq2 were used to calculate P values. **i**, Boxplot showing the abundance of representative cytokine genes in MEN1-high versus MEN1-low patient tumors in the TCGA LUAD cohort. Twenty patients with the highest and the lowest MEN1 expression were assigned to each group. Horizontal lines in the box represent the upper quartile, median and lower quartile from top to bottom. Vertical extending lines mark the 5th to 95th percentile (unpaired two-tailed Student's t-test). $^*P < 0.05$, $^{**}P < 0.01$. IgA, immunoglobulin A; IL, interleukin; P_{adj}, adjusted P value; Rep, replicate. **a**, Created with BioRender.com.

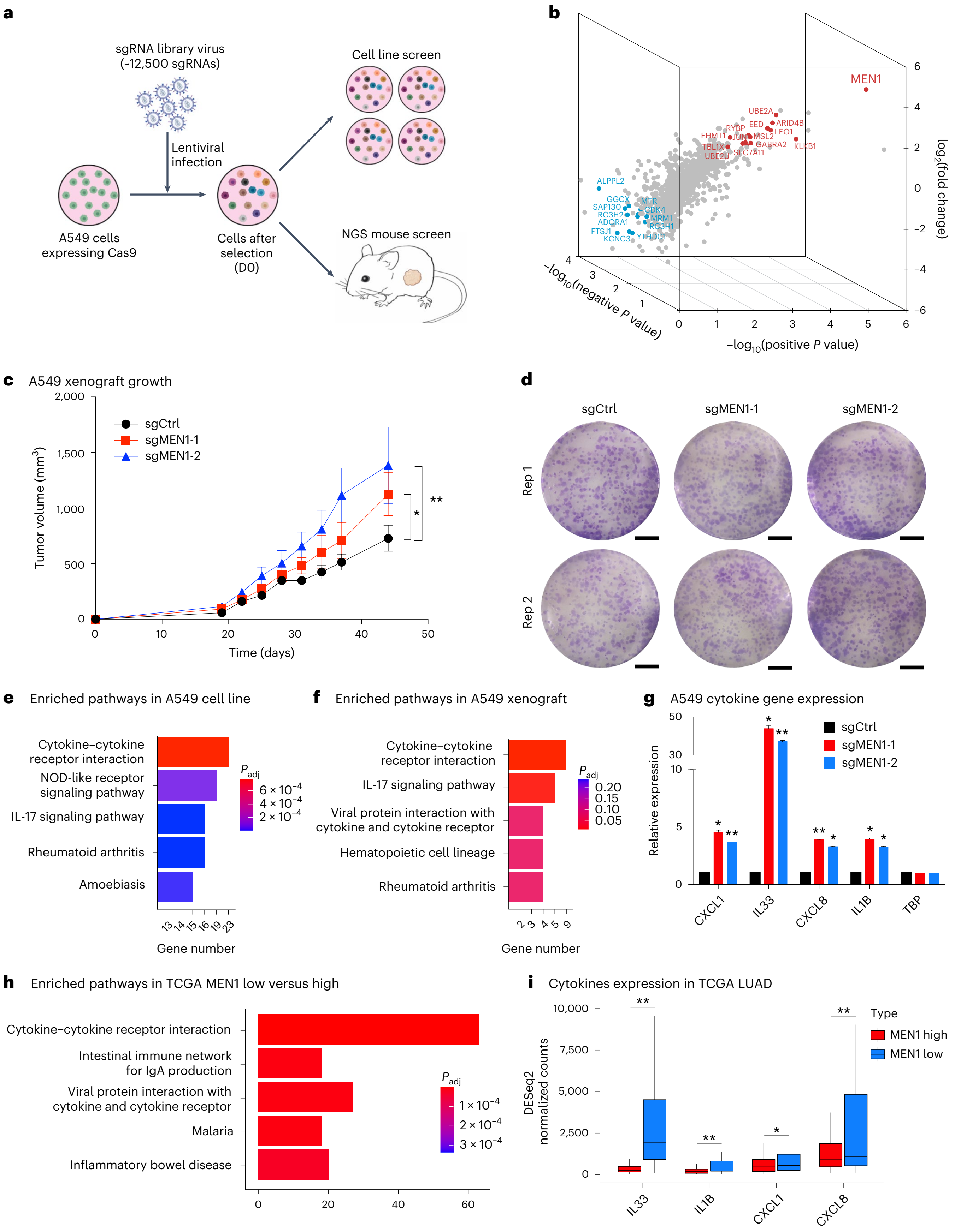
a
sgRNA library virus
(~12,500 sgRNAs)
Lentiviral
infection
A549 cells
expressing Cas9
Cells after
selection
(D0)
Cell line screen
NGS mouse screen
b
MEN1
UBE2A
ARID4B
EED
LEO1
RYBP
EHMT1
JUN
MSL2
TBL1X
GABRA2
KLKB1
SLC7A11
UBE2U
ALPPL2
GGCX
MTR
SAP130
CDK4
RC3H2
MRM1
ADORA1
RC3H1
FTSJ1
KCNC3
YTHDC1
−log10(negative P value)
−log10(positive P value)
log2(fold change)
c
A549 xenograft growth
Tumor volume (mm3)
Time (days)
sgCtrl
sgMEN1-1
sgMEN1-2
*
**
d
sgCtrl
sgMEN1-1
sgMEN1-2
Rep 1
Rep 2
e
Enriched pathways in A549 cell line
Cytokine–cytokine receptor interaction
NOD-like receptor signaling pathway
IL-17 signaling pathway
Rheumatoid arthritis
Amoebiasis
Padj
6 × 10−4
4 × 10−4
2 × 10−4
Gene number
f
Enriched pathways in A549 xenograft
Cytokine–cytokine receptor interaction
IL-17 signaling pathway
Viral protein interaction with cytokine and cytokine receptor
Hematopoietic cell lineage
Rheumatoid arthritis
Padj
0.20
0.15
0.10
0.05
Gene number
g
A549 cytokine gene expression
Relative expression
sgCtrl
sgMEN1-1
sgMEN1-2
CXCL1
IL33
CXCL8
IL1B
TBP
h
Enriched pathways in TCGA MEN1 low versus high
Cytokine–cytokine receptor interaction
Intestinal immune network for IgA production
Viral protein interaction with cytokine and cytokine receptor
Malaria
Inflammatory bowel disease
Padj
1 × 10−4
2 × 10−4
3 × 10−4
i
Cytokines expression in TCGA LUAD
DESeq2 normalized counts
Type
MEN1 high
MEN1 low
IL33
IL1B
CXCL1
CXCL8

We extended the gene expression analysis to patient tumors in The Cancer Genome Atlas (TCGA) LUAD RNA-seq dataset, contrasting the top and bottom 10% of patients based on MEN1 mRNA abundance (Extended Data Fig. 3e). In concordance with our observations in the A549 cell line, KEGG analysis identified 'cytokine–cytokine receptor interaction' as the top enriched term in the upregulated genes in MEN1-low patients (Fig. 1h,i, Extended Data Fig. 3f,g and Supplementary Table 4). These results suggest that MEN1 regulates the expression of cytokine-related genes in cell lines, PDX models and patient tumors.

MEN1 loss leads to MLL1 chromatin redistribution

Given that menin is a scaffolding protein involved in epigenetic regulation[30], we conducted a genome-wide cleavage under targets and release using nuclease (CUT&RUN)[31] assay to determine menin chromatin binding in A549 cells. The efficiency and specificity of the menin antibody was confirmed by immunoprecipitation and western blot analysis, as well as by chromatin immunoprecipitation–quantitative PCR (ChIP–qPCR) analysis of representative menin binding regions (Extended Data Fig. 4a,b, left). A total of 26,507 menin chromatin binding sites were identified using MACS[32] (Extended Data Fig. 4c,d and Supplementary Table 5). Binding and Expression Target Analysis (BETA)[33] revealed that although genes whose expression decreased upon menin depletion were significantly associated with menin binding, no enrichment was observed for upregulated genes, including the cytokine-related genes (Fig. 2a). Similar trends were obtained when applying BETA to differentially expressed genes in MEN1-low compared with MEN1-high subjects from the TCGA LUAD cohort (Extended Data Fig. 4e). These data suggest that the regulation of cytokine-related genes is not directly controlled by cis-regulation of menin.

Menin is known to interact with MLL1 to regulate target gene expression. Silencing of *MLL1* expression with two separate small interfering RNAs in A549 wild-type cells resulted in significant reductions in *CXCL1, IL33, CXCL8* and *IL1B* (Fig. 2b). Unlike *MLL1*, silencing of other methyltransferases or subunits within the MLL or *DOT1L1* complexes[29,34], including *MLL2, MLL3/4*, *UTX* and *DOT1L*, did not consistently activate the cytokine genes tested (Extended Data Fig. 4f–i). These data collectively suggest that menin-mediated regulation of these cytokine genes predominantly relies on *MLL1*. Indeed, induction of these cytokines in *MEN1* knockout cells was completely attenuated by silencing of *MLL1* (Fig. 2c).

We next expanded the CUT&RUN analysis to MLL1 in A549 cells with and without knockout of *MEN1* (Extended Data Fig. 4a,b, right). We identified more than 10,000 MLL1 chromatin binding sites in the control condition, with 68% overlapping with those of menin (Extended Data Fig. 4d (right), Supplementary Fig. 1a and Supplementary Table 5). Because MLL1 is a H3K4-specific methyltransferase, we extended our analysis to H3K4me3 histone modification (Supplementary Fig. 1b). H3K4me3 ChIP-seq in A549 cells identified approximately 30,000 H3K4me3 peak regions, and 55.6% of MLL1 binding overlap with these regions (Supplementary Fig. 1c,d). Differential binding analysis using MACS2 bdgdiff identified 1,857 regions with increased MLL1 binding and H3K4me3 signal, and 1,017 regions with decreased signal, in *MEN1* knockout cells (Fig. 2d and Supplementary Fig. 1e–g).

BETA indicated that the differential binding sites of H3K4me3 were not enriched near the upregulated genes upon *MEN1* knockout (Supplementary Fig. 1h), suggesting an indirect mechanism of regulation. Although the majority of the MLL1 binding sites were shorter than 500 bp and enriched in the promoter regions, we observed regions in the genome with strong binding intensities that exceeded 2 kb (Supplementary Fig. 1g). Because MACS is designed to identify short peaks, we used CREAM software to identify broad peaks[35]. This led to the identification of 422 broad regions ranging from 2 kb to 8 Mbp, most of which harbor repetitive elements and showed increased MLL1 occupancy upon MEN1 knockout (Extended Data Fig. 5a and Supplementary Table 5).

To determine whether loss of *MEN1* led to altered transcription of repetitive elements, we reanalyzed the A549 RNA-seq data by mapping the reads to repetitive genomic regions. Differential expression analysis identified 2,737 repeat loci with upregulated expression, and 865 repeat loci with downregulated expression (Fig. 2e). Most of the upregulated loci contained short interspersed nuclear elements(SINE), long interspersed nuclear elements (LINE) and simple repeats, with 740 of 2,737 located in the 442 CREAM peak regions (Fig. 2f and Extended Data Fig. 5b,c). Furthermore, the genomic regions with elevated MLL1 and H3K4me3 signals following *MEN1* depletion were significantly enriched in proximity to upregulated repeats, whereas the decreased ones were not (Fig. 2g and Extended Data Fig. 5d). ChIP–qPCR analysis of representative repeat regions showed that, whereas the binding of menin, UTX and H3K27me3 diminished upon *MEN1* depletion, there was a substantial increase in MLL1 binding and H3K4me3 signal at these repeat regions (Extended Data Fig. 5e–i).

Transcripts from repetitive genomic regions tend to form double-stranded RNA, such as inverted Alu repeat (Extended Data Fig. 5j). A significant induction of dsRNA staining was observed in MEN1 knockout compared with control A549 cells (Fig. 2h,i and Extended Data Fig. 5k, left). Transcription from repetitive genomic regions has been reported to induce DNA damage[36]. Indeed, significantly higher DNA damage, as indicated by stronger γ-H2AX staining, was observed upon *MEN1* knockout (Fig. 2j and Extended Data Fig. 5k (right)). dsRNA expression is known to induce interferon signaling. MEN1-low subjects in the TCGA LUAD cohort demonstrated a significantly higher level of interferon signaling genes compared with MEN1-high patients (Extended Data Fig. 5l). Furthermore, MEN1 knockout significantly induced the expression of ISG15 and IRF7 (Extended Data Fig. 5m). Together, these data suggest that *MEN1* knockout increases MLL1 occupancy at repetitive genomic regions, leading to the activation of dsRNA transcription.

Fig. 2 | MEN1 regulates MLL1 binding at repetitive genomic regions and transcription of dsRNA. a, Correlation between menin binding sites and target gene expression as evaluated by software BETA. **b**, RT–qPCR showing the abundance of representative cytokine-related genes with and without siRNA silencing of MLL1 in A549 cells. Housekeeping gene TBP was used as a control. Mean ± s.e.m. of two biological replicates is shown (unpaired two-tailed Student's *t*-test). $^{*}P < 0.05$, $^{**}P < 0.01$, $^{***}P < 0.001$. **c**, RT–qPCR performed in A549 cells with and without MEN1 deletion coupled with siRNA silencing of MLL1. Mean ± s.e.m. of four biological replicates is shown (unpaired two-tailed Student's *t*-test). $^{**}P < 0.01$, $^{***}P < 0.001$, $^{****}P < 0.0001$. **d**, Pileup plots showing H3K4me3 ChIP-seq and MLL1 CUT&RUN signal at 1,857 increased peak regions called by MACS2 bdgdiff. **e**, Heatmap showing repeat loci with differential expression in MEN1 knockout and control A549 cells in 2D culture. **f**, Donut plot showing the categories of upregulated repeats in MEN1 knockout A549 cells. **g**, Number of upregulated repeats within a given distance of the 1,857 peaks with increased H3K4me3 and MLL binding. Up-repeats are repeats that are significantly upregulated upon MEN1 knockout. Background are randomly selected repeat regions that did not show differential expression upon MEN1 knockout. The *P* value was calculated by one-sided paired *t*-test. **h**, Northern dot blot showing dsRNA staining in control and MEN1 knockout A549 xenograft tumors. The upper panel demonstrates dsRNA staining using the J2 antibody, and the lower panel illustrates staining of total RNA, serving as a loading control. The experiment was conducted using four biological replicates for each condition. **i**, Immunofluorescence imaging of control (sgCtrl) or MEN1 knockout (sgMEN1-1, sgMEN1-2) A549 cells or A549 cells treated with poly(I:C) for the detection of dsRNA (red). Red, dsRNA (J2 antibody); blue, DAPI. Scale bars, 20 µm. **j**, Immunofluorescence imaging of γ-H2AX of control or MEN1 knockout A549 cells or A549 cells. Green, γ-H2AX (γ-H2AX-antibody); blue, DAPI. Scale bars, 20 µm. ERV, endogenous retroviruses; ERVL, endogenous retroviral-like elements; hAT, hobo, Ac and Tam3; LTR, long terminal repeat; MaLR, mammalian apparent LTR-retrotransposons; TcMAR, Tc1/mariner .

MEN1 regulates tumor growth depending on mammalian apparent retroviral-like vesicles (MAVS) and cyclic GMP-AMP synthase (cGAS)–stimulator of interferon genes (STING)

dsRNA can induce a viral mimicry response via the RIG-1/MDA5-MAVS RNA sensing pathway or cGAS–cGAMP STING reverse-transcribed DNA sensing pathway[37–39], with Phosphorylation of TBK1 (p-TBK1) serving as an indicator of MAVS and/or cGAS–STING pathway activation[40]. Silencing of *MAVS* or *cGAS/STING* significantly attenuated the induction of cytokines in *MEN1* knockout cells (Fig. 3a and Extended Data Fig. 6a). In addition, *MEN1* knockout resulted in induction of p-TBK1 in *MEN1* knockout compared with control cells, whereas total TBK1 levels remained unchanged (Extended Data Fig. 6b).

In vivo analysis showed that *MAVS* or *cGAS* knockout in control cells had no noticeable effect on tumor growth (Extended Data Fig. 6c),

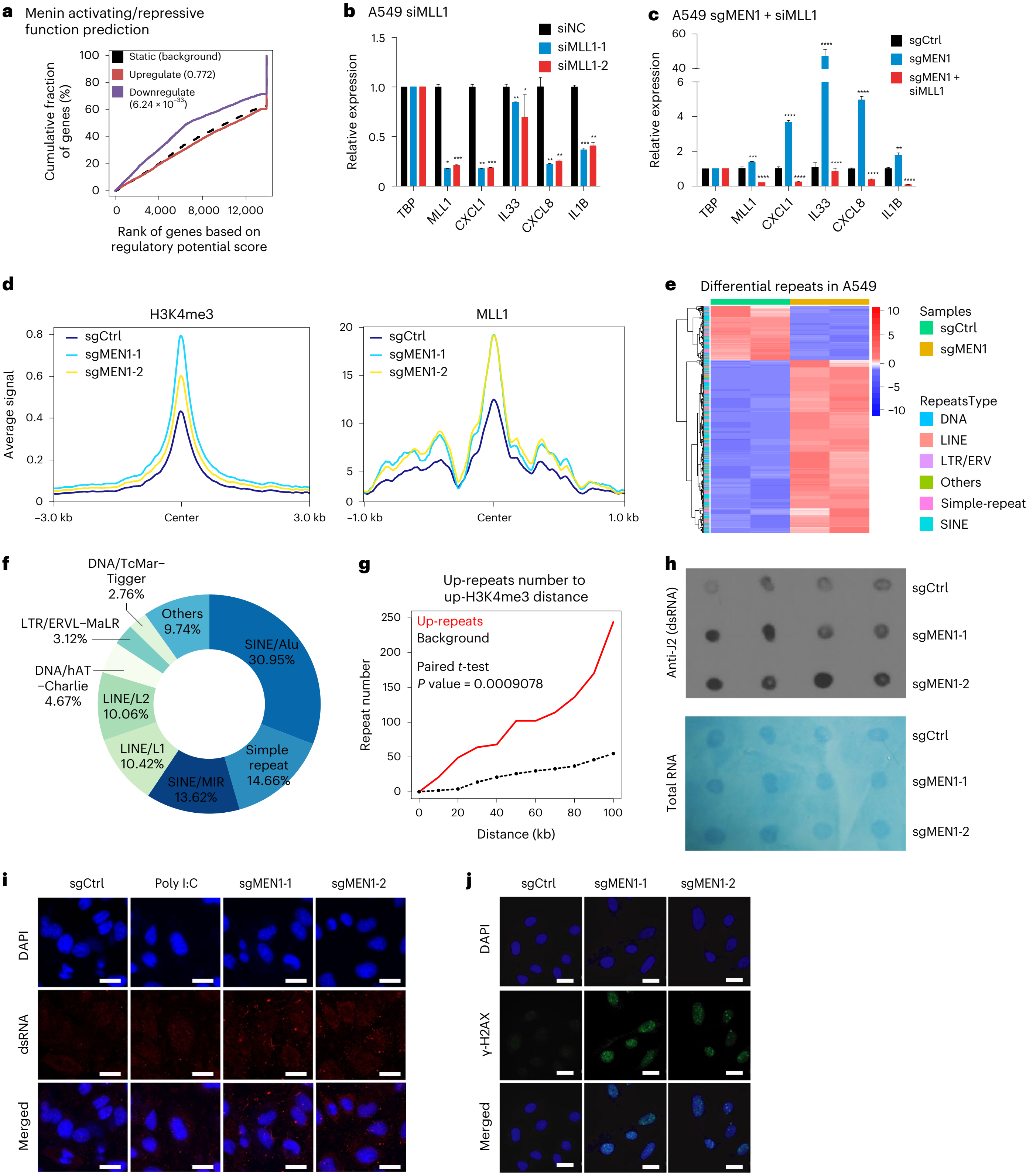

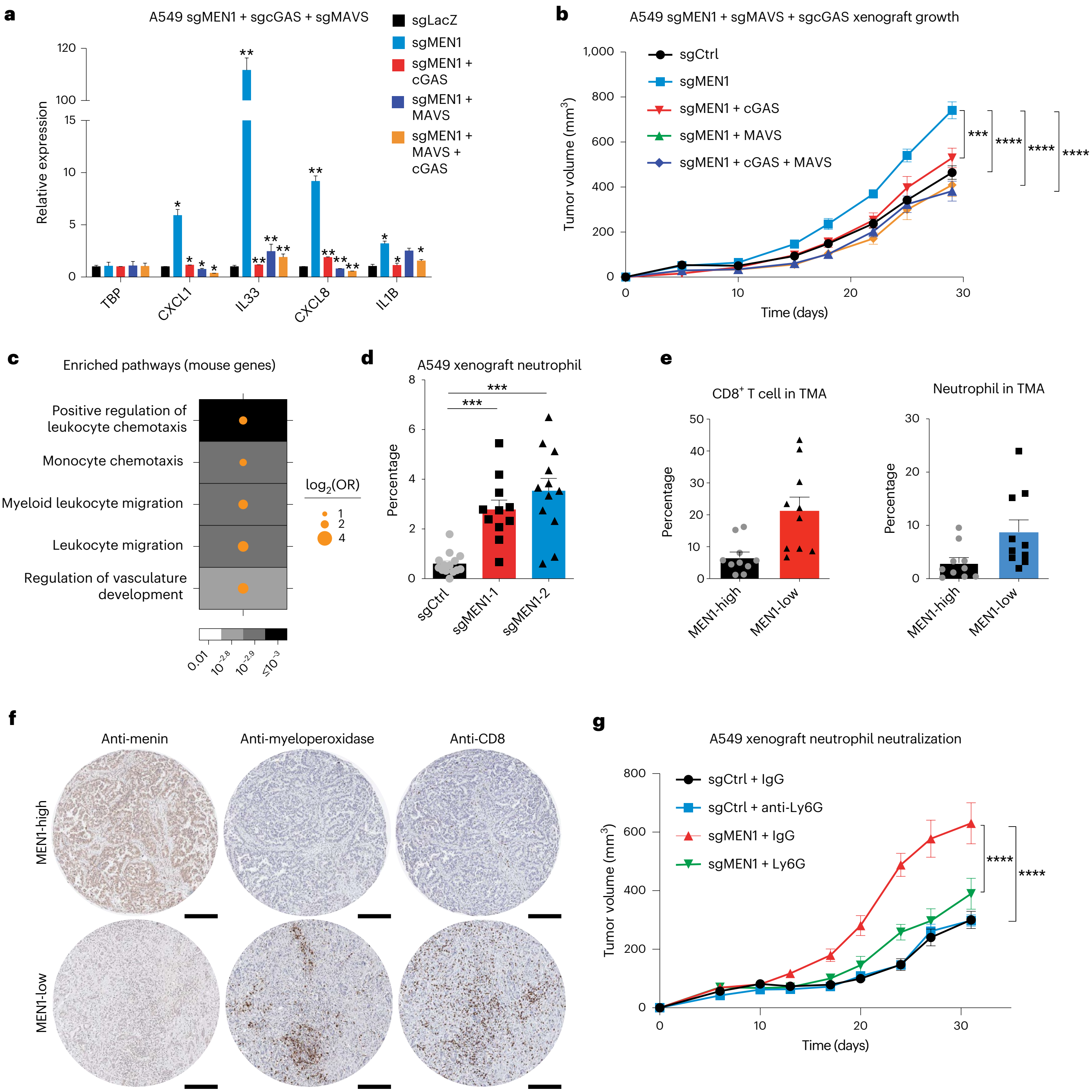

Fig. 3 | Antagonizing function of MEN1 and MLL1 in regulating cytokine gene signature and TME infiltration. a, RT–qPCR performed in A549 cells with and without MEN1 deletion coupled with deletion of MAVS and/or cGAS. Mean ± s.e.m. of two biological replicates is shown (unpaired two-tailed Student's *t*-test). $^*P < 0.05$, $^{**}P < 0.01$. **b**, A549 xenograft tumor growth rate in immunodeficient mice with and without knockout of MEN1 or in combination with MAVS and/or cGAS knockout. Each data point represents mean ± s.e.m. tumor volumes ($n = 10$ for each arm). Two-way ANOVA was used for statistical analysis. $^{***}P < 0.001$, $^{****}P < 0.0001$. **c**, Dot plot showing enriched KEGG terms of mouse differential genes from MEN1 knockout A549 xenografts. **d**, Quantification of neutrophil infiltration in A549 xenograft tumors with and without MEN1 deletion. Mean ± s.e.m. of neutrophil percentage from 12 tumors is shown (unpaired two-tailed Student's *t*-test). **e**, IHC staining showing percentage of neutrophil or CD8$^+$ T cells in MEN1-high versus MEN1-low tumor samples from a LUAD microarray (TMA). Mean ± s.e.m. of 20 tumors with the highest and the lowest MEN1 TMA scores were assigned to each group. $^{**}P < 0.01$, $^{***}P < 0.001$. **f**, Representative IHC staining images for MEN1, myeloperoxidase (neutrophil) and CD8 (CD8$^+$ T cell). Scale bars, 200 µm. **g**, A549 xenograft tumor growth rate in immunodeficient mice with and without knockout of MEN1 or in combination with anti-Ly6G antibody injection. Each data point represents mean ± s.e.m. tumor volumes ($n = 5$ for each arm). Two-way ANOVA was used for statistical analysis. OR, odds ratio.

but significantly reduced the induction of tumor growth in the *MEN1* knockout condition (Fig. 3b). These data suggest that *MEN1* regulates cytokine-related genes and tumor growth through a MAVS- and cGAS–STING-dependent viral mimicry mechanism.

MEN1 knockout induces neutrophil infiltration

To determine whether and how *MEN1* knockout modulates TME cell infiltration and interaction with tumor cells, we identified reads that specifically mapped to the mouse genome in the A549 xenograft tumor RNA-seq data. Differential gene and KEGG pathway analysis revealed a strong enrichment of terms related to leukocyte function in genes upregulated in *MEN1* knockout tumors (Fig. 3c and Extended Data Fig. 6d). Pathway analysis further demonstrated that the function of neutrophils, a subtype of leukocytes, is enriched in MEN1 knockout conditions (Extended Data Fig. 6e).

Immunohistochemistry (IHC) staining of anti-myeloperoxidase, a marker for neutrophil, revealed profound induction of neutrophil infiltration in *MEN1* knockout tumors compared with controls (Fig. 3d and Extended Data Fig. 6f). In addition, reanalysis of a publicly available RNA-seq dataset of leukemia xenograft tumors[41] revealed that menin inhibition induces cytokine gene expression and neutrophil infiltration in immunodeficient mice (Extended Data Fig. 6g,h).

To validate immune cell infiltrations in patient tumors, we performed IHC staining for neutrophil and CD8$^+$ T cells in a tissue microarray of the LUAD cohort. Tumors with lower MEN1 expression indeed exhibited much stronger neutrophil and CD8$^+$ T cell infiltration (Fig. 3e,f). Neutrophil neutralization with an antibody against myeloperoxidase significantly attenuated tumor growth induced by *MEN1* knockout in A549 xenografts (Fig. 3g), indicating that the tumor-promoting effect of *MEN1* knockout is dependent on neutrophils. Consistent with this, the percentage neutrophil infiltration in A549 xenograft tumors significantly increased with *MEN1* knockout but was reduced to baseline levels with knockout of *cGAS* or/and *MAVS* (Extended Data Fig. 6i).

MEN1 regulates tumor growth in an immune cell-dependent manner

Pan-cancer analysis using the TCGA datasets revealed that the 'cytokine–cytokine receptor interaction' gene signature is significantly higher in MEN1-low compared with MEN1-high patients in 26 of the 32 cancer (sub-)types analyzed (Extended Data Fig. 7a). The number and types of cytokine genes activated varied across different cancer types (Extended Data Fig. 7b).

Similar to A549 lung cancer cells, knockout of *MEN1* in colon cancer cell line HCT116 did not alter cell proliferation in vitro but significantly increased tumor growth in immunodeficient NSG mice (Fig. 4a,b and Extended Data Fig. 7c). Next, we extended our analysis to the CT26 mouse colon cancer cell line (Fig. 4c). Genetic ablation of *Men1* did not alter CT26 cell proliferation in vitro but led to significantly faster tumor growth in immunodeficient NSG mice (Fig. 4d and Extended Data Fig. 7d,e). Furthermore, significantly higher neutrophil infiltration was observed in *Men1* knockout tumors compared with controls (Extended Data Fig. 7f). By contrast, loss of Men1 resulted in significantly reduced tumor growth in immunocompetent mice (Fig. 4e). A similar effect was also observed in the syngeneic breast cancer model 4T1, with increased and decreased tumor growth upon *Men1* knockout in immunodeficient and immunocompetent mice, respectively (Extended Data Fig. 8a,b). We further extended the *Men1* knockout study to pancreatic cancer model HKP1 and prostate cancer model DKO, and consistently observed decreased tumor growth following *Men1* depletion in immunocompetent mice (Extended Data Fig. 8c–e).

To elucidate how the loss of *Men1* restricts CT26 tumor growth in immunocompetent mice, we transcriptionally profiled Men1-proficient and -deficient tumors. Differential gene analysis identified 350 upregulated and 309 downregulated genes, respectively, in the knockout compared with control conditions (Fig. 4f). Pathway analysis revealed activation of antiviral immune response pathways in Men1-deficient tumors (Fig. 4g and Extended Data Fig. 8f,g), indicating increased tumor immunogenicity. Cytokine-related genes with high expression levels in the MEN1-low colon cancer patient tumors were highly upregulated in Men1-deficient tumors of CT26, HKP1 and DKO (Extended Data Fig. 8h,i). The strong enrichment of virus response-related signatures further supports the role of *Men1* in suppressing viral mimicry, as observed in A549 cells. Indeed, *Men1* knockout exhibited strong upregulation of dsRNA species compared with control CT26 cells (Fig. 4h,i).

Men1 knockout increases CD8$^+$ T cell infiltration

To systematically investigate the TME populations affected by Men1 knockout, we conducted scRNA-seq and mass cytometry by time-of-flight (CyTOF) analysis of Men1-proficient and -deficient CT26 tumors grown in immunocompetent mice (Extended Data Fig. 9a), using standard data processing and quality control procedures[42,43]. Analysis of transcriptomic profiles of 7,595 cells identified 7 cell types with 16 distinct sub-clusters (Fig. 5a, Extended Data Fig. 9b,c and Supplementary Fig. 2). The proportion of macrophages and T cells significantly increased in *Men1* knockout tumors (Fig. 5b and Extended Data Fig. 9d). These data suggest that *Men1* knockout impacts immune cell infiltration.

To further characterize the enhanced immune response upon *Men1* knockout in immunocompetent mice, we profiled 606,301 CD45$^+$ immune cells from CT26 tumors with CyTOF using an antibody panel targeting 35 immune markers (Fig. 5c, Extended Data Fig. 9e and Supplementary Table 6). We observed an overall increase in the percentage of immune cells in Men1-deficient tumors (Fig. 5d and Extended Data Fig. 9f). In addition to the overall increase in CD45$^+$ cells, the relative composition of the immune cells also changed, with a significant enrichment of CD8$^+$ T cells, dendritic cells and a subset of macrophages (Fig. 5d and Extended Data Fig. 9g). To further validate the impact of *MEN1* knockout on CD8$^+$ T cells, we established A549 xenografts in humanized NSG mice, which were reconstituted with a human immune system. *MEN1* knockout resulted in significantly reduced tumor growth (Extended Data Fig. 9h), in contrast to the increased tumor growth in nonhumanized NSG mice (Fig. 1c). IHC staining revealed significantly increased CD8$^+$ T infiltration in *MEN1* knockout tumors compared with control tumors (Extended Data Fig. 9i,j). Similarly, IHC analysis of CT26 tumors with Men1 depletion also showed increased CD8$^+$ T cell infiltration (Fig. 5e), findings that are consistent with the scRNA-seq and CyTOF analysis.

Pharmacological inhibition of menin reduces tumor growth

Pharmacologic inhibition of the menin–MLL interaction is an effective treatment in preclinical models and clinical trials of MLL1-rearranged and NPM1-mutant leukemias[44–46]. To assess the efficacy of inhibiting menin in solid cancer types, we treated CT26 cancer cells with the clinical stage menin inhibitor ziftomenib (KO-539)[46]. In line with the Men1 knockout phenotype, we observed a dose-dependent induction of representative cytokine genes in CT26 following ziftomenib treatment (Fig. 6a), validating the on-target effect of ziftomenib in these cells. In addition, *cGAS* or *MAVS* deletion attenuated ziftomenib treatment-induced upregulation of cytokine genes (Extended Data Fig. 10a). Consistently, ziftomenib treatment also results in an increase in phosphorylated Tbk1 (Extended Data Fig. 10b). Enhanced cytokine expression was consistently detected in lung and pancreatic cancer explant PDX tissues and organoid models following treatment with ziftomenib (Extended Data Fig. 10c–f). To further confirm the effect of ziftomenib on chromatin dynamics, we conducted MLL1 and H3K4me3 ChIP assays in wild-type A549 cells treated with either dimethyl sulfoxide or ziftomenib. Ziftomenib treatment significantly reduced menin abundance (Extended Data Fig. 10g). ChIP–qPCR analysis validated significantly increased MLL1 and H3K4me3 signals at selected repeat

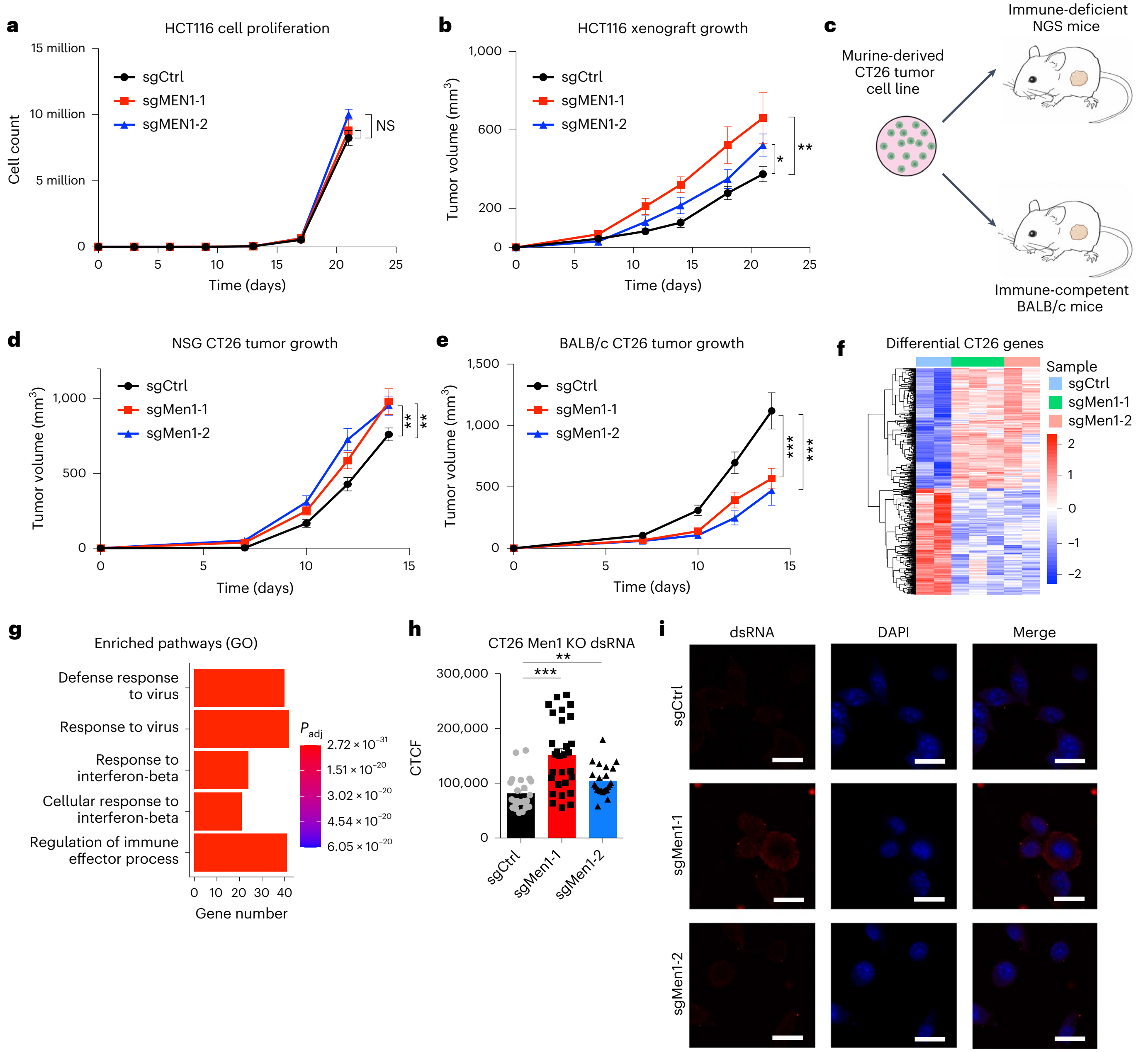

Fig. 4 | Immunocompetence-dependent tumor-promoting and -inhibiting function of MEN1 in colon cancer. a, Cell proliferation rate of HCT116 in 2D cell culture with and without knockout of MEN1. NS, not significant. Each data point represents mean ± s.e.m. cell counts ($n = 3$ for each arm). Two-way ANOVA was used for statistical analysis. **b**, HCT116 xenograft tumor growth rate in immunodeficient mice with and without knockout of MEN1. Each data point represents mean ± s.e.m. tumor volumes ($n = 5$ for each arm). Two-way ANOVA was used for statistical analysis. $^{*}P < 0.05$, $^{**}P < 0.01$. **c**, Schematic view of murine CT26 engraftment experiment design. **d**, Tumor growth in immunodeficient NSG mice inoculated with control (sgEV) or Men1 knockout (sgMen1-1, sgMen1-2) CT26 cells. Each data point represents mean ± s.e.m. tumor volumes ($n = 12$ for each arm). $^{**}P < 0.01$. **e**, Tumor growth in immunocompetent BALB/c mice inoculated with control (sgEV) or Men1 knockout (sgMen1-1, sgMen1-2) CT26 cells. Each data point represents mean ± s.e.m. tumor volumes ($n = 5$ for each arm). Two-way ANOVA was used for statistical analysis. $^{***}P < 0.001$. **f**, Heatmap showing expression value (z-score based on DESeq normalized RNA-seq counts) of differential genes from Men1 knockout versus control tumors in immunocompetent mice. Two control samples and four Men1 knockout tumors were subjected to RNA-seq analysis. **g**, GO analysis of differentially expressed genes in Men1 knockout versus control cells was performed and the top five terms are shown. The x axis represents the number of genes. Wald tests defined in DEseq2 were used to calculate P values. **h**,**i**, Quantification (**h**) and representative immunofluorescence images (**i**) of control (sgCtrl) or Men1 knockout (KO) CT26 cells for the detection of dsRNA. Red signal, dsRNA (J2 antibody); blue signal, DAPI. Scale bars, 20 µm. Each bar in the left-hand panel represents the mean of quantifications from 30 randomly picked fields (unpaired two-tailed Student's t-test). $^{**}P < 0.01$, $^{***}P < 0.001$. CTCF, corrected total cell fluorescence.

regions tested, consistent with that observed with CRISPR mediated *MEN1* depletion (Extended Data Fig. 10h).

In concordance with *Men1* knockout, drug treatment significantly reduced tumor growth compared with the control treatment in a dosage-dependent manner (Fig. 6b). Ziftomenib treatment had a similar growth inhibitory effect in the syngeneic 4T1 breast cancer allograft model in immunocompetent mice (Extended Data Fig. 10i,j). A significantly increased tumor growth rate was observed in the pancreatic cancer PDX model OCIP200 in immunodeficient mice following ziftomenib treatment (Extended Data Fig. 10k), consistent with

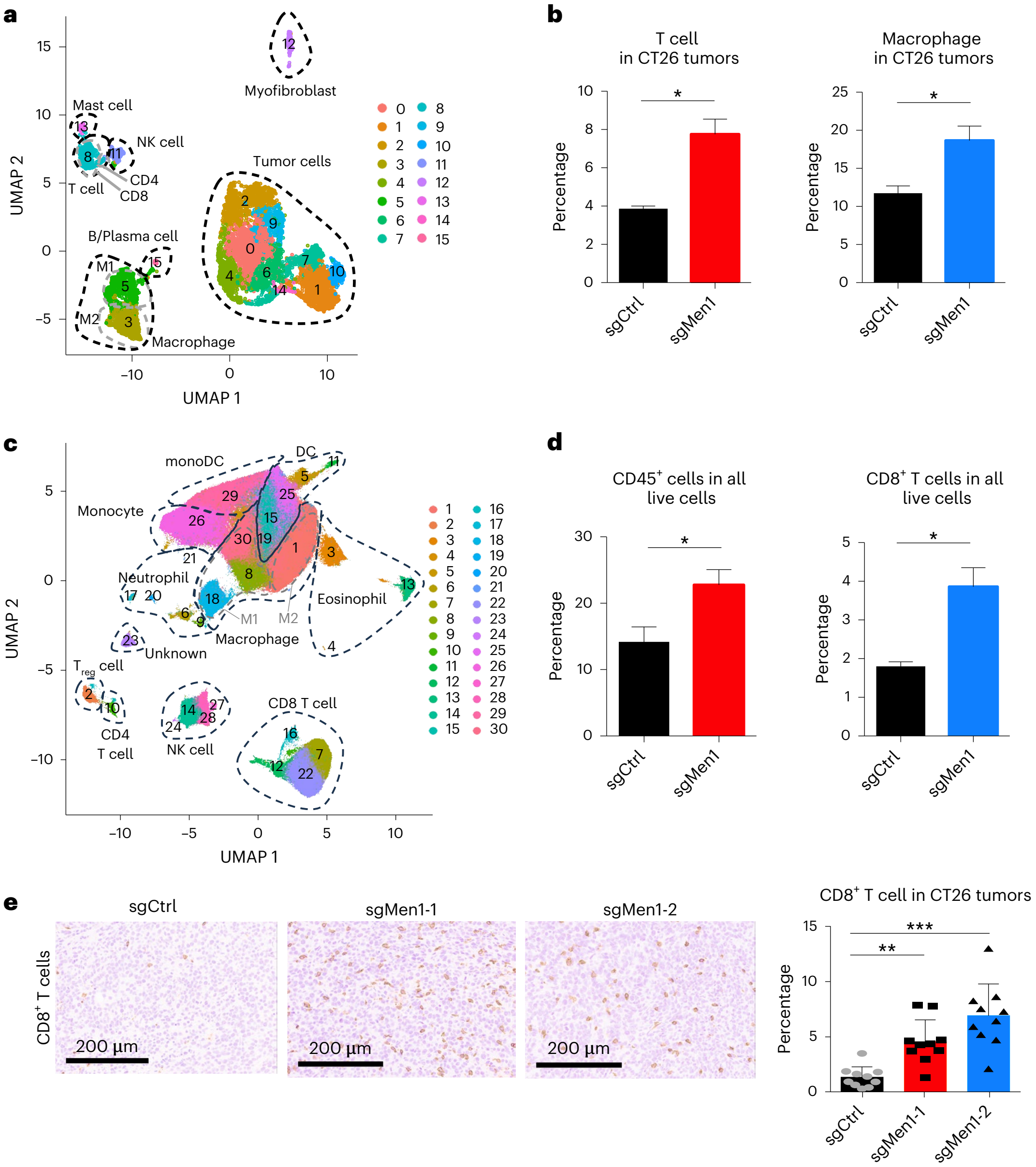

Fig. 5 | scRNA-seq, CyTOF and IHC analysis confirmed increased immune cell infiltration in Men1 knockout CT26 tumors. **a**, UMAP view of 7,595 single cells from scRNA-seq profiling of CT26 tumors with and without depletion of Men1, color coded by assigned clusters. Dotted circles mark cell types as determined by relevant marker genes. **b**, Percentages of T cells and macrophages in control (sgCtrl) and Men1 knockout (sgMen1-1, sgMen1-2) CT26 tumor samples. Mean ± s.e.m. of two to four biological replicates are shown (unpaired two-tailed Student's *t*-test). $^{*}P < 0.05$ **c**, UMAP view of 606,301 single cells from CyTOF profiling of 10 CT26 tumors with and without depletion of Men1. **d**, Percentage of $CD45^{+}$ cells (left) and $CD8^{+}$ T cells (right) of live cells captured by CyTOF. Mean ± s.e.m. of four biological replicates (sgCtrl) for control and six biological replicates for Men1 knockout (sgMen1) are shown (unpaired two-tailed Student's *t*-test). **e**, Representative IHC images (left) and quantifications (right) showing the abundance of $CD8^{+}$ T cells in control (sgCtrl) and Men1 knockout (sgMen1-1, sgMen1-2) CT26 tumors. Mean ± s.e.m. of quantifications from 10 tumor IHC sections are shown (unpaired two-tailed Student's t-test). $^{**}P < 0.01$, $^{***}P < 0.001$. Scale bars, 200 µm. DC, dendritic cells; NK cell, natural killer cell.

the TME-dependent effects observed with *MEN1* genetic depletion. Furthermore, treatment with ziftomenib resulted in a marked increase in $CD8^{+}$ T cell infiltration, with stronger induction observed at a higher dosage (Fig. 6c). Although $CD8^{+}$ T cell neutralization alone had no obvious effect on tumor growth in the control condition, it completely abolished the tumor-suppressive effect of ziftomenib (Fig. 6d), suggesting that MEN1 regulation of tumor growth depends on $CD8^{+}$ T cells and that menin blockade might constitute a new immunotherapeutic approach.

Bulk RNA-seq showed significantly higher levels of Cd274/PD-L1 and a trend of increased Pdcd1/PD-1 expression in Men1-depleted CT26 xenograft tumors and MEN1-low patient tumors in the TCGA LUAD cohort (Fig. 6e), likely due to increased immune cell infiltrations. scRNA-seq and CyTOF showed that a subset of tumor and macrophage cells express PD-L1, and the $CD8^{+}$ T cells express high levels of PD-1, with a modest increase in the knockout tumors (Supplementary Fig. 3a–e). Ziftomenib or anti-PD-1 treatment alone substantially reduced the CT26 tumor growth and the combination demonstrated a significantly stronger effect (Fig. 6f). These data suggest that pharmacological inhibition of menin alone or in combination with immunotherapy may benefit patients with functional menin protein (Fig. 6g).

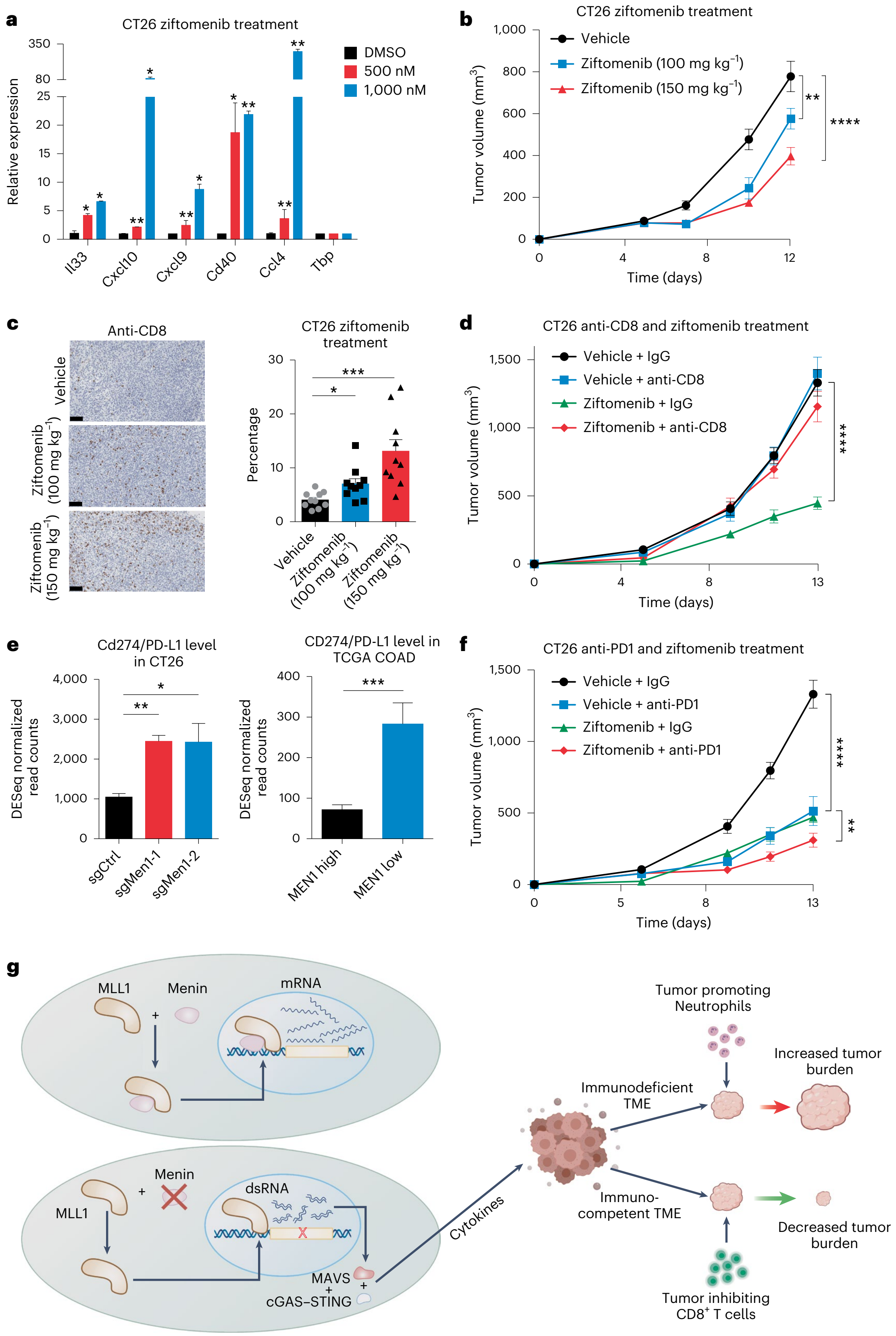

Discussion

Tumors develop within a complex microenvironment and identifying clinically relevant therapeutic targets amid such complexity is a daunting task. In this study, we used parallel in vitro and in vivo CRISPR knockout screens to identify genes that modulate tumor and TME interactions. We found that the epigenetic regulator MEN1 markedly influences tumor growth under certain conditions in vivo, but does not affect cell growth in vitro.

MEN1 plays a complex multifaceted role in cancer. It is a well-characterized tumor suppressor, loss of which causes multiple

Fig. 6 | Pharmacological inhibition of MEN1 reduces tumor growth in a CD8$^+$ T cell-dependent manner and demonstrates additive effect with anti-PD-1 treatment. a, RT–qPCR showing the relative expression of cytokine-related genes in CT26 cells treated with different dosages of menin inhibitor ziftomenib. Mean ± s.e.m. of two biological replicates are shown (unpaired two-tailed Student's *t*-test). **b**, CT26 tumor growth with vehicle control or ziftomenib treatment at dosages of 100 and 150 mg kg^{-1}. Each data point represents mean ± s.e.m. tumor volumes ($n = 5$ for each arm). Two-way ANOVA was used for statistical analysis. $^*P < 0.05$, $^{**}P < 0.01$, $^{***}P < 0.001$. **c**, Representative IHC images (left) and quantifications (right) showing the infiltration of CD8$^+$ T cells in CT26 tumors with vehicle control and KO5-39 treatment. Scale bars, 100 µm. Mean ± s.e.m. of quantifications from 10 tumor IHC sections are shown (unpaired two-tailed Student's *t*-test). $^*P < 0.05$, $^{***}P < 0.001$. **d**, Tumor growth rate in immunocompetent mice inoculated with CT26 cells following IgG or CD8 antibody treatment in combination with vehicle control or ziftomenib (150 mg kg^{-1}). Each data point represents mean ± s.e.m. tumor volumes ($n = 10$ in each group). Two-way ANOVA was used for statistical analysis. $^{***}P < 0.001$. **e**, Relative abundance of Cd274/PD-L1 in CT26 tumors with and without deletion of Men1 from bulk RNA-seq data (left). Mean ± s.e.m. of two biological replicates are shown (unpaired two-tailed Student's *t*-test). Relative abundance of CD274/PD-L1 in MEN1-high and MEN1-low patient tumors in the TCGA COAD cohort (right). Mean ± s.e.m. of 50 patient tumors with the highest and the lowest MEN1 expression were shown (unpaired two-tailed Student's *t*-test). $^*P < 0.05$, $^{**}P < 0.01$, $^{***}P < 0.001$. **f**, Tumor growth rate in immunocompetent mice inoculated with CT26 cells following IgG or PD-1 antibody treatment in combination with vehicle control or ziftomenib (150 mg kg^{-1}). Each data point represents mean ± s.e.m. tumor volumes ($n = 10$ in each group). $^{**}P < 0.01$, $^{****}P < 0.0001$. **g**, Schematic view of the dual function of MEN1 in modulating tumor–microenvironment interactions. MEN1 suppression reshapes MLL1 chromatin binding, triggering cytokine gene expression via MAVS- and cGAS-dependent viral mimicry response. Consequently, this leads to increased infiltration of tumor-promoting neutrophils and tumor-inhibiting CD8$^+$ T cells in immunodeficient and immunocompetent conditions, respectively. DMSO, dimethyl sulfoxide. **g**, Created with BioRender.com.

endocrine neoplasia type 1 and development of lung, prostate, skin and central nerve system tumors[47–50]. Paradoxically, however, *MEN1* also functions as an oncogene, notably in acute myeloid leukemia with NPM1 mutations of MLL1-rearrangements[46,51]. As a chromatin adapter, menin is known to directly interact with the N-terminal domain of H3K4-specific methyltransferase MLL1/MLL2. Our study reveals the existence of an antagonist role for menin, distinct from its previously described cofactor functions. Menin accomplishes this role potentially by squelching MLL1 in the COMPASS complex, resulting in reduced MLL1–chromatin interactions at repetitive genomic regions and subsequent suppression of cytokine-related gene expression. In addition, although menin–MLL1 coactivated target genes vary in different tissues, the suppression of cytokine signaling is highly consistent across different tissues and species, suggesting a highly conserved and common mechanism.

Insertion of transposable elements resulted in a complex distribution of interspersed repeats comprising almost half of the human genome[52,53]. The transcribed interspersed repeats form dsRNA, which is sensed by the RIG-1/MDA5-MAVS signaling pathway or reverse-transcribed and detected via the cGAS–cGAMP STING pathway[37], leading to increased innate immune responsiveness through a viral mimicry mechanism[38,39,54–57]. Our data show that upon *MEN1* depletion, MLL1 activates cytokine signals at least partially *via* the MAVS and cGAS–STING pathways. The potential cooperative effects of these epigenetic regulators warrant further exploration.

The immunocompetence-dependent tumor-inhibiting and -promoting function provides a mechanism underlying the paradoxical function of *MEN1*. Several inhibitors that block menin–MLL interactions have entered clinical development in acute myeloid leukemia[25,26]. Our data suggest that menin inhibition may also offer therapeutic value related to activation of the immune response in solid tumors. Because infiltrating immune cells may have both tumor-promoting and -inhibiting effects, the efficacy of menin inhibition will likely be context-specific. Additional studies identifying biomarkers predicting the efficacy are warranted.

In summary, our study presents a mechanism contributing to the paradoxical tumor-suppressive and oncogenic function of *MEN1* and provides a strong rationale for targeting menin alone or in combination with immunotherapy for both hematologic and solid cancer.

Online content

Any methods, additional references, Nature Portfolio reporting summaries, source data, extended data, supplementary information, acknowledgements, peer review information; details of author contributions and competing interests; and statements of data and code availability are available at https://doi.org/10.1038/s41588-024-01874-9.

References

1. Jin, M.-Z. & Jin, W.-L. The updated landscape of tumor microenvironment and drug repurposing. *Signal Transduct. Target Ther.* **5**, 166 (2020).
2. Mantovani, A., Allavena, P., Sica, A. & Balkwill, F. Cancer-related inflammation. *Nature* **454**, 436–444 (2008).
3. Hanahan, D. & Weinberg, R. A. Hallmarks of cancer: the next generation. *Cell* **144**, 646–674 (2011).
4. Balkwill, F. R., Capasso, M. & Hagemann, T. The tumor microenvironment at a glance. *J. Cell Sci.* **125**, 5591–5596 (2012).
5. Qian, J. et al. A pan-cancer blueprint of the heterogeneous tumor microenvironment revealed by single-cell profiling. *Cell Res.* **30**, 745–762 (2020).
6. Wu, S. Z. et al. A single-cell and spatially resolved atlas of human breast cancers. *Nat. Genet.* **53**, 1334–1347 (2021).
7. Thorsson, V. et al. The immune landscape of cancer. *Immunity* **48**, 812–830.e14 (2018).
8. Tang, L. et al. Nanoparticle-mediated targeted drug delivery to remodel tumor microenvironment for cancer therapy. *Int. J. Nanomed.* **16**, 5811–5829 (2021).
9. Shalem, O. et al. Genome-scale CRISPR–Cas9 knockout screening in human cells. *Science* **343**, 84–87 (2014).
10. Wang, T., Wei, J. J., Sabatini, D. M. & Lander, E. S. Genetic screens in human cells using the CRISPR–Cas9 system. *Science* **343**, 80–84 (2014).
11. Henriksson, J. et al. Genome-wide CRISPR screens in T helper cells reveal pervasive crosstalk between activation and differentiation. *Cell* **176**, 882–896.e18 (2019).
12. Manguso, R. T. et al. In vivo CRISPR screening identifies Ptpn2 as a cancer immunotherapy target. *Nature* **547**, 413–418 (2017).
13. Shifrut, E. et al. Genome-wide CRISPR screens in primary human T cells reveal key regulators of immune function. *Cell* **175**, 1958–1971 (2018).
14. Tsherniak, A. et al. Defining a cancer dependency map. *Cell* **170**, 564–576.e16 (2017).
15. Jin, V., Wang, J. & Tang, B. *Integration of Multisource Heterogenous Omics Information in Cancer* (Frontiers Media SA, 2020).
16. Pacini, C. et al. Integrated cross-study datasets of genetic dependencies in cancer. *Nat. Commun.* **12**, 1661 (2021).
17. Wang, X. et al. In vivo CRISPR screens identify the E3 ligase Cop1 as a modulator of macrophage infiltration and cancer immunotherapy target. *Cell* **184**, 5357–5374.e22 (2021).
18. Li, F. et al. In vivo epigenetic CRISPR screen identifies *Asf1a* as an immunotherapeutic target in *Kras*-mutant lung adenocarcinoma. *Cancer Discov.* **10**, 270–287 (2020).

19. Gao, S. et al. CRISPR screens identify cholesterol biosynthesis as a therapeutic target on stemness and drug resistance of colon cancer. *Oncogene* **40**, 6601–6613 (2021).
20. Soares, F. et al. CRISPR screen identifies genes that sensitize AML cells to double-negative T-cell therapy. *Blood* **137**, 2171–2181 (2021).
21. Chen, S. et al. Genome-wide CRISPR screen in a mouse model of tumor growth and metastasis. *Cell* **160**, 1246–1260 (2015).
22. Li, W. et al. MAGeCK enables robust identification of essential genes from genome-scale CRISPR/Cas9 knockout screens. *Genome Biol*. **15**, 554 (2014).
23. Meyers, R. M. et al. Computational correction of copy number effect improves specificity of CRISPR–Cas9 essentiality screens in cancer cells. *Nat. Genet*. **49**, 1779–1784 (2017).
24. Love, M. I., Huber, W. & Anders, S. Moderated estimation of fold change and dispersion for RNA-seq data with DESeq2. *Genome Biol*. **15**, 550 (2014).
25. Perner, F. et al. MEN1 mutations mediate clinical resistance to menin inhibition. *Nature* **615**, 913–919 (2023).
26. Issa, G. C. et al. The menin inhibitor revumenib in KMT2A-rearranged or NPM1-mutant leukaemia. *Nature* **615**, 920–924 (2023).
27. Sparbier, C. E. et al. Targeting Menin disrupts the KMT2A/B and polycomb balance to paradoxically activate bivalent genes. *Nat. Cell Biol*. **25**, 258–272 (2023).
28. Soto-Feliciano, Y. M. et al. A molecular switch between mammalian MLL complexes dictates response to Menin-MLL inhibition. *Cancer Discov*. **13**, 146–169 (2023).
29. Lin, J. et al. Menin 'reads' H3K79me2 mark in a nucleosomal context. *Science* **379**, 717–723 (2023).
30. La, P. et al. Tumor suppressor menin: the essential role of nuclear localization signal domains in coordinating gene expression. *Oncogene* **25**, 3537–3546 (2006).
31. Skene, P. J. & Henikoff, S. An efficient targeted nuclease strategy for high-resolution mapping of DNA binding sites. *eLife* **6**, e21856 (2017).
32. Zhang, Y. et al. Model-based analysis of ChIP-Seq (MACS). *Genome Biol*. **9**, R137 (2008).
33. Wang, S. et al. Target analysis by integration of transcriptome and ChIP-seq data with BETA. *Nat. Protoc*. **8**, 2502–2515 (2013).
34. Soto-Feliciano, Y. M. et al. Molecular switch between mammalian MLL complexes dictates response to Menin-MLL inhibition. *Cancer Discov*. **13**, 146–169 (2023).
35. Madani Tonekaboni, S. A., Haibe-Kains, B. & Lupien, M. Large organized chromatin lysine domains help distinguish primitive from differentiated cell populations. *Nat. Commun*. **12**, 499 (2021).
36. Chen, R., Ishak, C. A. & De Carvalho, D. D. Endogenous retroelements and the viral mimicry response in cancer therapy and cellular homeostasis. *Cancer Discov*. **11**, 2707–2725 (2021).
37. Gao, D. et al. Cyclic GMP–AMP synthase is an innate immune sensor of HIV and other retroviruses. *Science* **341**, 903–906 (2013).
38. Roulois, D. et al. DNA-demethylating agents target colorectal cancer cells by inducing viral mimicry by endogenous transcripts. *Cell* **162**, 961–973 (2015).
39. Morel, K. L. et al. EZH2 inhibition activates a dsRNA–STING–interferon stress axis that potentiates response to PD-1 checkpoint blockade in prostate cancer. *Nat. Cancer* **2**, 444–456 (2021).
40. Liu, S. et al. Phosphorylation of innate immune adaptor proteins MAVS, STING, and TRIF induces IRF3 activation. *Science* **347**, aaa2630 (2015).
41. Borkin, D. et al. Pharmacologic inhibition of the Menin-MLL interaction blocks progression of MLL leukemia in vivo. *Cancer Cell* **27**, 589–602 (2015).
42. Chen, S. et al. Single-cell analysis reveals transcriptomic remodellings in distinct cell types that contribute to human prostate cancer progression. *Nat. Cell Biol*. **23**, 87–98 (2021).
43. Xu, W. et al. Early innate and adaptive immune perturbations determine long-term severity of chronic virus and *Mycobacterium tuberculosis* coinfection. *Immunity* **54**, 526–541.e7 (2021).
44. Krivtsov, A. V. et al. A Menin-MLL inhibitor induces specific chromatin changes and eradicates disease in models of MLL-rearranged leukemia. *Cancer Cell* **36**, 660–673.e11 (2019).
45. Grembecka, J. et al. Menin-MLL inhibitors reverse oncogenic activity of MLL fusion proteins in leukemia. *Nat. Chem. Biol*. **8**, 277–284 (2012).
46. Davis, J. A. et al. Clinical-stage menin inhibitor KO-539 is synergistically active with multiple classes of targeted agents in KMT2A-r and NPM1-mutant AML models. *Blood* **138**, 3357 (2021).
47. Al-Salameh, A., Cadiot, G., Calender, A., Goudet, P. & Chanson, P. Clinical aspects of multiple endocrine neoplasia type 1. *Nat. Rev. Endocrinol*. **17**, 207–224 (2021).
48. Qiu, H. et al. MEN1 deficiency leads to neuroendocrine differentiation of lung cancer and disrupts the DNA damage response. *Nat. Commun*. **11**, 1009 (2020).
49. Chandrasekharappa, S. C. et al. Positional cloning of the gene for multiple endocrine neoplasia-type 1. *Science* **276**, 404–407 (1997).
50. Jiao, Y. et al. DAXX/ATRX, MEN1, and mTOR pathway genes are frequently altered in pancreatic neuroendocrine tumors. *Science* **331**, 1199–1203 (2011).
51. Yokoyama, A. & Cleary, M. L. Menin critically links MLL proteins with LEDGF on cancer-associated target genes. *Cancer Cell* **14**, 36–46 (2008).
52. Lander, E. S. et al. Initial sequencing and analysis of the human genome. *Nature* **409**, 860–921 (2001).
53. Payer, L. M. & Burns, K. H. Transposable elements in human genetic disease. *Nat. Rev. Genet*. **20**, 760–772 (2019).
54. Babaian, A. & Mager, D. L. Endogenous retroviral promoter exaptation in human cancer. *Mob. DNA* **7**, 24 (2016).
55. Deblois, G. et al. Epigenetic switch-induced viral mimicry evasion in chemotherapy-resistant breast cancer. *Cancer Discov*. **10**, 1312–1329 (2020).
56. Sheng, W. et al. LSD1 ablation stimulates anti-tumor immunity and enables checkpoint blockade. *Cell* **174**, 549–563.e19 (2018).
57. Chiappinelli, K. B. et al. Inhibiting DNA methylation causes an interferon response in cancer via dsRNA including endogenous retroviruses. *Cell* **162**, 974–986 (2015).

[1]Department of Medical Biophysics, University of Toronto, Toronto, Ontario, Canada. [2]Princess Margaret Cancer Centre, University Health Network, Toronto, Ontario, Canada. [3]Department of Laboratory Medicine, Shanghai Pulmonary Hospital, Tongji University School of Medicine, Shanghai, China. [4]Department of Immunology, University of Toronto, Toronto, Ontario, Canada. [5]Institute of Precision Medicine, The First Affiliated Hospital, Sun Yat-sen University, Guangzhou, China. [6]Ludwig Institute for Cancer Research, Nuffield Department of Medicine, University of Oxford, Oxford, UK. [7]Department of Laboratory Medicine and Pathobiology, University of Toronto, Toronto, Ontario, Canada. [8]Department of Thoracic Surgery, Shanghai Pulmonary Hospital, Tongji University School of Medicine, Shanghai, China. [9]Kura Oncology Inc, San Diego, CA, USA. [10]Department of Molecular Genetics, University of Toronto, Toronto, Ontario, Canada. [11]Centre for Molecular and Systems Biology, Lunenfeld-Tanenbaum Research Institute, Mount Sinai Hospital, Toronto, Ontario, Canada. [12]Present address: West China School of Public Health and West China Fourth Hospital, and State Key Laboratory of Biotherapy, Sichuan University, Chengdu, China. [13]These authors contributed equally: Peiran Su, Yin Liu, Tianyi Chen. ✉e-mail: Ming.Tsao@uhn.ca; hansenhe@uhnresearch.ca

Methods

All samples obtained in this study complied with the relevant ethical regulations approved by the institutional ethics committee and Research Ethics Board at the University Health Network (UHN).

Western blotting

Cells were lysed in RIPA buffer containing phosphatase and protease inhibitor cocktails (Roche, cat. no. 11697498001). Protein was quantified using a bicinchoninic acid assay. Secondary antibodies were used at a 1:5,000 dilution. Primary antibodies were diluted according to the manufacturers' recommended ratios. Used antibodies included anti-menin (Bethyl Laboratories, cat. no. A300-105A), anti-MLL1 (Abcam, cat. no. ab272023), anti-H4K4me3 (Abcam, cat. no. ab8580), anti-UTX (Bethyl Laboratories, cat. no. A302-374A), anti-cGAS (Cell Signaling Technology, cat. no. 151025), anti-MAVS (Abcam, cat. no. ab89825), anti-TBK1 (Cell Signaling Technology, cat. no. 3504T), anti-pTBK1 (Cell Signaling Technology, cat. no. 5483T), GAPDH (Santa Cruz Biotechnology, cat. no. sc-47724) and Vinculin (Cell Signaling Technology, cat. no. 13901S), H3 (Cell Signaling Technology, cat. no. 4499L) and β-tubulin (Cell Signaling Technology, cat. no. 2128S).

CUT&RUN assays

In total, 250,000 cells per condition were washed twice with 1 ml of wash buffer by pelleting for 3 min at 600*g*. As previously described[58], the cells were bound to Concanavalin A magnetic beads (Cell Signaling Technology, cat. no. 93569S) using nuclear binding buffer and incubated at room temperature on a rotator at 15 rpm for 10 min. Antibodies (anti-menin (Bethyl Laboratories, cat. no. A300-105A) and anti-MLL1 (Abcam, cat. no. ab272023)), were diluted to a ratio of 1:100 using antibody buffer. After the 10-min incubation, the samples were placed on a magnetic separator. The nuclear binding buffer was removed and the antibody mixture was added to the bead-bound samples. Samples were incubated overnight at 4 °C on a rotator. Following overnight incubation, pAG-MNAse enzyme (Cell Signaling Technology, cat. no. 40366S) was diluted 1:1,000 in digitonin buffer. The samples were placed on a magnetic separator, supernatant was removed and pAG-MNAse buffer was added. The samples were mixed on a rotator (15 rpm) and incubated at 4 °C for 1 h. To activate the pAG-MNAse, 3 µl of cold 100 mM $CaCl_2$ was added and the samples were incubated on ice for 30 min. After 30 min, stop buffer was immediately added to quench the pAG-MNAse reaction. DNA fragments were released from the cells by incubating at 37 °C for 10 min with 700 rpm shaking, followed by a 5-min centrifugation at 16,000*g* at 4 °C. Supernatant containing DNA fragments was moved to a new tube containing 3 µl of 10% SDS and 2.5 µl of Proteinase K (Thermo Fisher Scientific, cat. no. EO0492) then incubated for 10 min at 70 °C. The DNA fragments were purified using phenol–chloroform extraction. Purified DNA was quantified via Qubit and 7.5 ng was used for input into the library preparation. Library preparation was completed following the Takara SMARTer ThruPLEX DNA-Seq protocol (Takara Bio, cat. no. R400676). Samples were amplified using 11 PCR cycles as determined via qPCR. Final library traces were generated using the Agilent 2100 Bioanalyzer and quantified via qPCR before sequencing. Libraries were sequenced to a depth of 50–60 million reads per sample using paired-end 50 sequencing configuration on Illumina's NovaSeq 6000.

Chromatin immunoprecipitation assay

ChIP assays on A549 cells were conducted as previously described[59], both with and without MEN1 knockdown. In brief, 5 million cells underwent crosslinking with 1% formaldehyde for 10 min at room temperature, followed by quenching with 125 mM glycine. Subsequently, the cell pellets were twice washed with cold PBS buffer and resuspended in 300 µl of modified RIPA buffer (10 mM Tris–HCl pH 8, 1 mM EDTA, 140 mM NaCl, 1% Triton X-100, 0.1% SDS, 0.1% sodium deoxycholate) supplemented with protease inhibitor. The resuspended pellet underwent sonication for 18 cycles (30 s on, 30 s off) at 4 °C using Bioruptor (Diagenode).

Following sonication, the cell lysate was precleared with 40 µl of protein A/G beads before incubation with antibody-coated beads at 4 °C overnight. To prepare the antibody-coated beads, 5 µg of target antibody of interest were incubated with 11 µl of protein A and 11 µl of protein G beads (Thermo Fisher Scientific, cat. no. 10002D and 10004D) with rotation for at least 6 h at 4 °C. Antibodies used for ChIP assays included anti-menin (Bethyl Laboratories, cat. no. A300-105A), anti-MLL1 (Abcam, cat. no. ab272023), anti-H3K27me3 (Abcam, cat. no. ab6002), anti-H4K4me3 (Abcam, cat. no. ab8580) and anti-UTX (Bethyl Laboratories, cat. no. A302-374A).

After incubation, beads underwent a series of washes: once with 0.5 ml of modified RIPA buffer, once with high salt modified RIPA buffer (NaCl increased to 500 mM), once with LiCl buffer (10 mM Tris–HCl pH 8, 1 mM EDTA, 250 mM LiCl, 0.5% NP-40, 0.1% sodium deoxycholate) on a rotator for 5 min each at 4 °C, and finally twice with 0.5 ml of TE buffer (pH 8). The beads were then resuspended in 100 µl of de-crosslinking buffer (1% SDS, 0.1 M $NaHCO_3$). Subsequently, 1 µl of RNase A (Thermo Fisher Scientific, cat. no. EN0531) was added, and the mixture was incubated at 37 °C for 30 min with shaking, followed by incubation at 55 °C for 30 min with shaking in the presence of 2 µl of Proteinase K (Thermo Fisher Scientific, cat. no. AM2546). The crosslinking was reversed by incubating at 65 °C overnight with shaking. DNA purification was carried out using the PCR purification kit (Qiagen, cat. no. 28004), and the purified DNA was then subjected to qPCR or Illumina ChIP-Seq library construction using the ThruPLEX DNA-seq kit (Takara, cat. no. R400676).

sgRNA pooled library design and synthesis

The Epi-Drug library consists of ~12,500 sgRNAs targeting 317 epigenetic regulators, 657 US Food and Drug Administration-approved drug targets based on DrugBank 4.3 (ref. 60), and control genes, with 10 sgRNAs per gene on average (Supplementary Table 1). The sgRNAs were designed using the CRISPR-DO tool that accounted for sgRNA specificity and cutting efficiency[61]. sgRNAs were synthesized as 73-base polymer/oligonucleotides (CustomArray). After being amplified by PCR, the PCR product was purified and cloned in the lentiGuide-Puro vector using BsmBI (NEB). Ligation was performed using the NEBuilder HiFi DNA Assembly Cloning Kit and transformed into an electrocompetent stain (Stbl4; Thermo Fisher Scientific) to achieve ~300× coverage. Colonies were scraped off agar plates with LB medium. Plasmid DNA was extracted using a NA0310 Sigma GenElute HP Plasmid Maxiprep Kit and adequate library representation of each sgRNA was confirmed by NGS.

CRISPR–Cas9 screening, sequencing and analysis

Library viruses were produced in HEK293FT cells and multiplicity of infection was determined for the A549 cell line as previously described[9]. The Cas9-expressing A549 cell line was infected with the library at an multiplicity of infection of ~0.3 and coverage of >200×. At 24 h post-infection, cells were selected with puromycin for 72 h (1 µg ml^{-1}) and then cultured for ~21 days in Petri dishes or subcutaneously inoculated into mice for ~21 days. Day 0 genomic DNA was harvested after 3 days of puromycin selection. Genomic DNA was extracted and sgRNA inserts were amplified by PCR as previously described[62]. Screens were performed in duplicate, and the libraries were sequenced on an Illumina HiSeq2500.

The NGS data from CRISPR screens were first aligned to the library sgRNAs using bowtie. The resulting count matrix was the input to the tool MAGeCK[22], which estimates the enrichment/depletion of individual sgRNAs using a negative binomial model and estimates the enrichment of genes using the robust ranking aggression model.

Mouse tumor growth experiments

Four- to six-week-old male NSG, C57BL6 and BALB/c mice were maintained at the UHN Animal Resources Centre. NSG, C57BL6 or BALB/c mice were injected subcutaneously with 50 µl of a single-cell suspension containing 5×10^5 MEN1/Men1 knockout and control A549, HCT116, CT26, 4T1, HKP1 or DKO cells. Syngeneic CT26, 4T1 models were injected subcutaneously in 50 µl of a single-cell suspension into BALB/c mice. Cryo-preserved OCIP200 PDX tissues were implanted subcutaneously in NSG mice. The tumors were expanded in mouse replicates ($n = 10$) to evaluate the agent ziftomenib. Once tumors had initiated growth, the vehicle or drug was administered daily by oral gavage. To generate humanized mice, human peripheral blood mononuclear cells were engrafted into NSG pups after the pups had been irradiated at 1 Gy. Ten to twelve weeks after the injection, blood samples were collected from the mice, and human immune cell engraftment was determined by flow cytometry. Humanized mice with engraftment efficiency (percent human CD45$^+$/(percent human CD45$^+$ + percent mouse CD45$^+$)) values between 20% and 50% were used in subsequent A549 xenograft experiments. Mouse weight and tumor volume were measured twice weekly. Xenograft (tum) or sizes were measured twice per week. Tumor volumes were calculated using the formula: tumor volume (mm^3) = $L \times W^2/2$, where L is the major axis (largest cross-sectional diameter) of the tumor and W is the minor axis. The data are presented as the mean ± s.e.m. Mice were sacrificed when the diameter of the tumor reaches 1.5 cm. All procedures were performed in accordance with the International Guidelines for the Use of Animals and approved by the Animal Care Committee at UHN.

Gene knockout and transfection

Guide RNA plasmids targeting MEN1 was constructed into a lentiCRISPR V2-Blast vector (Addgene, cat. no. 83480). Guide RNA plasmids targeting MAVS and cGAS were constructed in a lentiCRISPR V2 vector (Addgene, cat. nos. 83480, 98291, 98290). siRNAs were transfected into the cancer cells by RNAiMAX reagent (Thermo Fisher Scientific, cat. no. 13778075), following the manufacturer's protocol. siRNAs used in this study were ordered from Thermo Fisher Scientific and sequences are listed in Supplementary Table 7.

Statistical analyses and reproducibility

Statistical analyses for in vitro and in vivo assays were performed using GraphPad Prism v.6 (GraphPad Software). Data were expressed as mean ± s.e.m. Two-tailed unpaired Student's t-test and one-way analysis of variance (ANOVA) were performed to identify significant differences between groups in our experiments. R v.3.3.0 was used to perform statistical analysis. Details of the test method used for statistical analysis is specified in the relevant figure captions and Methods. All values were considered significantly different at $P < 0.05$. Western blotting for MEN1 knockout samples was performed in biological replicates.

RNA-seq mapping and data processing

RNA was extracted with TRIzol reagent (Thermo Fisher Scientific, cat. no. 15596026) and processed using a RNA-seq library preparation kit (Illumina, cat. no. RS-122-2101) to produce libraries for deep sequencing on NextSeq. Library preparation and sequencing were performed according to the manufacturer's protocol. RNA-seq raw reads were first filtered by trim_galore (v.0.5.0) then mapped to the human genome (hg38) using STAR (v.2.4.2a)[63] software with default parameters. The hg38 GENCODE gene list was used for all transcription level analysis. RNA-seq reads strands were determined by RSeQC (v.2.6.1)[64,65]. HTSeq (v.0.11.0)[66] was used to obtain gene-level read counts from STAR-mapped bam files. The resultant gene read count table was subjected to DESeq2 (v.1.22.2)[24] for differential gene analysis and a false discovery rate cutoff of 0.01 was chosen to identify significant differential genes. A $\log_2$(fold change) value less than −1 and a $\log_2$(fold change) value above 1 were chosen as upregulated genes and downregulated genes, respectively.

For visualization of RNA-seq data, we generated bedGraph files using genomeCoverageBed function in the BEDTools suite with signal scaled to reads per 10 million for both plus and minus strands. The bedGraph files were converted to bigwig format using the bedGraphToBigWig function in the BLAT suite.

CUT&RUN and ChIP-seq mapping and data processing

CUT&RUN and ChIP-seq reads were mapped to the human genome (hg38) using bowtie. MACS2 callpeak was used for peak calling with the parameter '–SPMR' on. MACS2[32] bdgdiff was used to call differential peaks. Resultant bedgraph files were converted to big wiggle files with the bedGraphToBigWig function. CREAM[67] was applied to call broad peak regions followed by the removal of ENCODE blacklist regions.

Gene Ontology analysis

Gene Ontology (GO) and KEGG analyses were performed using R package clusterProfiler v.3.10.1 (ref. 68). Terms with a false discovery rate <0.01 were considered significantly enriched. A complete list of terms enriched can be found in the supplementary datasets.

BETA analysis

BETA (v.1.0.7)[33] software was used to predict menin directly regulated genes by combining menin binding peaks and differentially expressed genes.

Repeats analysis

The human repeat masker file was downloaded from the website (http://www.repeatmasker.org/genomes/hg38/RepeatMasker-rm405-db20140131/hg38.fa.out.gz). The reference file was converted to bed format using bedops/2.4.37. RNA-seq reads were remapped to genome hg38 by STAR (v.2.4.2a)[63] with parameter –outFilterMultimapNMax set to 100 and –winAnchorMultimapNmax set to 100. Exon reads were calculated by HTSeq (v.0.11.0)[66]. Exons with more than five reads were subtracted from the repeats masker file by running bedtools (v.2.27.1)[69] subtract. Read counts on repeat regions were calculated by bedtools (v.2.27.1)[69] multicov. DESeq2 was used to call differential repeats.

Immunofluorescence confocal microscopy

A549 cells constitutively expressing Cas9 protein were infected with lentivirus containing sgRNA targeting LacZ or MEN1. A round coverslip was loaded to a 24-well plate and incubated with 1 ml of 100% ethanol for 5 min at room temperature. After one wash with PBS buffer, 75,000 cells in growth media were seeded to each well. The plates were incubated at 37 °C overnight to allow attachment of the cells to the coverslip. The next day, the medium was aspirated, and the cells were washed once with PBS and fixed with ice cold methanol for 15 min at −20 °C. The cells were washed three times with PBS and blocked with 1% bovine serum albumin in PBS at room temperature for 1 h. Primary antibody targeting dsRNA (J2; Scicons, cat. no. 10010500) and γ-H2AX (EMD Millipore, cat. no. JBW30) diluted with blocking solution at a ratio of 1:500 was added to each well, and the plates were incubated at 4 °C overnight with shaking. The next day, the diluted antibodies were aspirated, and the cells were washed three times with PBS for 10 min at room temperature with shaking. The cells were then incubated with the secondary antibody (anti-mouse immunoglobulin G (IgG) (H+L), F(ab′)$_2$ fragment (Alexa Fluor 647 conjugate; Cell Signaling Technology, cat. no. 4410s) diluted with blocking solution at a ratio of 1:1,000 in a dark environment for 1 h at room temperature with shaking. The cells were washed three times with PBS in a dark environment at room temperature for 10 min with shaking. The coverslips were mounted to glass slides with ProLong Gold Antifade Mountant with 4′,6-diamidino-2-phenylindole (DAPI) (Thermo Fisher Scientific, cat. no. P36935). Confocal microscopy was performed with Zeiss LSM700 (oil ×40 magnification) and ImageJ software was used to analyze the images acquired. Corrected total cell fluorescence was calculated as: corrected total cell fluorescence = integrated density − (area of selected cell × mean fluorescence of background readings).

Tumor dissociation to single cells

Fresh tumor samples were harvested from mice and minced into small, approximately 1-mm, cubic pieces on ice. The samples were washed five times with PBS and enzymatically digested in DMEM/F12 media containing 1× collagenase/hyaluronidase (STEMCELL Technologies, cat. no. 07912) and 5% FBS buffer for 2 h at 37 °C with rotation. After dissociation, samples were centrifuged at 350*g* for 5 min. After the supernatant was removed, 5 ml of 0.25% Trypsin-EDTA (STEMCELL Technologies, cat. no. 07901) was added to the pelleted cells followed by incubate for 5 min at 37 °C. Then 10 ml of cold modified Hanks' balanced salt solution buffer (HBSS modified; STEMCELL Technologies, cat. no. 37150) supplemented with 2% FBS was added to the solution followed by centrifugation for 5 min. After the supernatant was removed, 1 ml of dispase (STEMCELL Technologies, cat. no. 07913) in 5 mg ml^{-1} and 100 µl of DNase I (STEMCELL Technologies, cat. no. 07900) in 1 mg ml^{-1} were added to the cell pellets and were pipetted up and down with a 27 G syringe five times. The cell pellet was resuspended in 10 ml of HBSS modified buffer supplemented with 2% FBS and filtered through a 40µm cell strainer (STEMCELL Technologies, cat. no. 27305). The product can be washed with the appropriate buffer and is ready for CyTOF or scRNA-seq.

Mass cytometry by time-of-flight

Details of each antibody are listed Supplementary Table 7. Purified unconjugated antibodies were labeled with metal tags at the SickKids-UHN Flow and Mass Cytometry Facility using a MaxPar Antibody Labeling kit (Fluidigm). Directly conjugated antibodies were purchased from Fluidigm. All working antibody concentrations were determined by titration.

Single-cell suspensions from individual samples were washed with PBS and pulsed with 12.5 µM cisplatin (Fluidigm) in PBS for 1 min before quenching with CyTOF staining media (Mg+/Ca+ HBSS containing 2% FBS (Multicell), 10 mM HEPES (Corning) and FBS underlay). Cells were then fixed for 12 min at room temperature with transcription factor fixative (Bioscience, cat. no. 00-5523-00), permeabilized and individual samples were barcoded according to manufacturer's instructions (Fluidigm 20-Plex Pd Barcoding Kit, cat. no. 201060), before being combined. Combined samples were resuspended in staining media containing metal-tagged surface antibodies and Fc block (Bioxcell, cat. no. CD16/32) for 30 min at 4 °C. Cells were washed, then permeabilized and stained with metal-tagged intracellular antibodies using a transcription factor staining buffer set. Cells were incubated in PBS containing 0.3% (w/v) saponin (Sigma, cat,. no. S7900-25G), 1.6% (v/v) paraformaldehyde (Polysciences) and 50 nM iridium (Fluidigm) for 1 h at room temperature. Cells were analyzed on a Helios or Helios2 mass cytometer (Fluidigm) at the SickKids-UHN Flow and Mass Cytometry Facility. EQ Four Element Calibration Beads (Fluidigm) were used to normalize signal intensity over time using CyTOF software v.6.7. Flow cytometry standard files were manually debarcoded and analyzed using Cytobank6.2 (Cytobank).

Data were pre-transformed by ArcSinh transformation (cofactor = 5) in R. Phenogragh analysis was performed with R package 'Cytofkit'[70,71] (seeds = 42, k = 30). Uniform manifold approximation and projection (UMAP) analysis was performed using the R package 'UMAP'[72] with default settings. Differential states and differential abundance were calculated using the limma and edgeR tests, respectively, with the R package 'diffcyt'[73]. An adjusted P value <0.05 was considered significant for the comparisons made. Median signal intensity values were used to generate heatmaps. Heatmaps were generated in R using the blue–red, plasma or viridis color packages and the R package 'gplots'.

scRNA sequencing (10X Genomics)

Cell capture and complementary DNA synthesis was carried out using the Single Cell 3′ Library and Gel Bead Kit V2 (10X Genomics, cat. no. 120237) and a Chromium Single Cell A Chip Kit (10X Genomics, cat. no. 120236). The cell suspension (300–600 living cells per microliter) was loaded onto the chromium single-cell controller (10X Genomics) to generate single-cell gel beads in the emulsion, according to the manufacturer's protocol. In short, single cells were suspended in PBS containing 0.04% bovine serum albumin. Approximately 7,000 cells were added to each channel, and the target cell recovery rate was estimated to be 3,000 cells. Captured cells were lysed and the released RNA was barcoded through reverse transcription in individual gel beads in emulsion.

Using an S1000TM Touch Thermal Cycler (Bio-Rad) to reverse transcribe, the gel beads in emulsion were programmed at 53 °C for 45 min, followed by 85 °C for 5 min, then held at 4 °C. Complementary DNA was generated and then amplified, and the quality was assessed using an Agilent 4200 system.

For scRNA-seq library preparation, according to the manufacturer's protocol, scRNA-seq libraries were constructed using a Single Cell 3′ Library Gel Bead Kit V2. Sequencing was performed on an Illumina NovaSeq 6000 sequencer with a sequencing depth of at least 100,000 reads per cell and 150-bp (PE150) paired-end reads.

Data analysis and visualization

Data analysis was conducted using R (v.3.4.1). Data visualization was conducted using ggplot2 (v.3.1.0). Figures 1a and 6g and Extended Data Fig. 10a were created using BioRender.com.

Reporting summary

Further information on research design is available in the Nature Portfolio Reporting Summary linked to this article.

Data availability

Raw sequencing data of CRISPR screening, RNA-seq, ChIP-seq and CUT&RUN can be accessed at the NCBI Gene Expression Omnibus (GEO) repository under the accessions GSE194349 (CRISPR screening), GSE194355 (A549 RNA-seq), GSE197595 (CT26 RNA-seq), GSE194353 (MEN1 and MLL1 CUT&RUN) and GSE194354 (H3K4me3 ChIP-seq). Source data are provided with this paper.

Code availability

All R packages used are available online as described in the Methods. No custom code was used for any aspect of data processing or analysis.

References

58. Linares-Saldana, R. et al. BRD4 orchestrates genome folding to promote neural crest differentiation. *Nat. Genet.* **53**, 1480–1492 (2021).
59. Wei, Z. et al. MYC reshapes CTCF-mediated chromatin architecture in prostate cancer. *Nat. Commun.* **14**, 1787 (2023).
60. Law, V. et al. DrugBank 4.0: shedding new light on drug metabolism. *Nucleic Acids Res.* **42**, D1091–D1097 (2014).
61. Ma, J. et al. CRISPR-DO for genome-wide CRISPR design and optimization. *Bioinformatics* **32**, 3336–3338 (2016).
62. Wang, T., Lander, E. S. & Sabatini, D. M. Viral packaging and cell culture for CRISPR-based screens. *Cold Spring Harb. Protoc.* **2016**, db.prot090811 (2016).
63. Dobin, A. et al. STAR: ultrafast universal RNA-seq aligner. *Bioinformatics* **29**, 15–21 (2013).
64. Wang, L., Wang, S. & Li, W. RSeQC: quality control of RNA-seq experiments. *Bioinformatics* **28**, 2184–2185 (2012).
65. Wang, L. et al. Measure transcript integrity using RNA-seq data. *BMC Bioinformatics* **17**, 58 (2016).
66. Anders, S., Pyl, P. T. & Huber, W. HTSeq—a Python framework to work with high-throughput sequencing data. *Bioinformatics* **31**, 166–169 (2015).

67. Tonekaboni, S. A. M., Mazrooei, P., Kofia, V., Haibe-Kains, B. & Lupien, M. Identifying clusters of cis-regulatory elements underpinning TAD structures and lineage-specific regulatory networks. *Genome Res.* **29**, 1733–1743 (2019).
68. Yu, G., Wang, L.-G., Han, Y. & He, Q.-Y. clusterProfiler: an R package for comparing biological themes among gene clusters. *OMICS* **16**, 284–287 (2012).
69. Quinlan, A. R. & Hall, I. M. BEDTools: a flexible suite of utilities for comparing genomic features. *Bioinformatics* **26**, 841–842 (2010).
70. Chen, H. et al. Cytofkit: a bioconductor package for an integrated mass cytometry data analysis pipeline. *PLoS Comput. Biol.* **12**, e1005112 (2016).
71. Levine, J. H. et al. Data-driven phenotypic dissection of aml reveals progenitor-like cells that correlate with prognosis. *Cell* **162**, 184–197 (2015).
72. McInnes, L., Healy, J., Saul, N. & Großberger, L. UMAP: uniform manifold approximation and projection. *J. Open Source Softw.* **3**, 861 (2018).
73. Weber, L. M., Nowicka, M., Soneson, C. & Robinson, M. D. diffcyt: differential discovery in high-dimensional cytometry via high-resolution clustering. *Commun. Biol.* **2**, 183 (2019).

Acknowledgements

We thank T. Wu for providing primer sequences for repeat analysis, and the Princess Margaret Genomic Centre for support of CRISPR screen, CUT&RUN and high-throughput sequencing. This work was supported by the Princess Margaret Cancer Foundation (grant no. 886012001223 to H.H.H.), Natural Sciences and Engineering Research Council of Canada discovery grant (grant no. 498706 to H.H.H.), Canada Institutes of Health Research (CIHR) project grants (grant nos. 142246, 152863, 152864 and 159567 to H.H.H., and 438793 to D.S. and H.H.H.), CIHR Foundation (grant no. FDN-148395 to M.-S.T.), Terry Fox New Frontiers Program Project Grants (grant no. 1090 P3 to H.H.H. and A.B., and 1124 to H.H.H.), National Natural Science Foundation of China (grant no. 31801111 to Y.L.), Dream Mentor-Outstanding Young Talents Program of Shanghai Pulmonary Hospital (grant no. fkyq1910 to Y.L.), 2021 Shanghai 'Medical Garden Rising Stars' Young Medical Talents of Shanghai Municipal Health Commission Award (talent plan to Y.L.), Shanghai Pujiang Program (grant no. 22PJD063 to Y.L.), China Scholarship Council (grant no. 201906265006 to Y.L.). D.S. is supported by a tier 2 Canadian Research Chair. H.H.H. is supported by a tier 1 Canadian Research Chair. H.H.H. holds Joey and Toby Tanenbaum Brazilian Ball Chair in Prostate Cancer. Kuro Oncology, Inc. provided menin inhibitor ziftomenib and research funding for this project.

Author contributions

P.S., Y.L., M.-S.T. and H.H.H. designed the experiments. P.S., Y.L., T.C., J.H., B.X.W., S.F., N.A., R.K., Y.X., M.T., X.C., M.G., M.Y.H., S.W., F.S., P.M., X.X., M.K. and N.-A.P. performed the experiments. Y.L., P.S., Y.X., Y.Z., G.Z., S.C., V.C., P.H.H., W.X., C.C., F.B., C.O., F.Y., M.L., S.H., B.H.L., R.H., A.B., D.D.C., D.G.B., D.S., S.A.M., M.-S.T. and H.H.H. analyzed the data. Y.L., P.S., M.-S.T. and H.H.H. wrote the first draft of the manuscript. All authors revised and approved the manuscript.

Competing interests

F.B. is Vice President of Translational Research of Kura Oncology, Inc. The other authors declare no competing interests.

Additional information

Extended data is available for this paper at https://doi.org/10.1038/s41588-024-01874-9.

Supplementary information The online version contains supplementary material available at https://doi.org/10.1038/s41588-024-01874-9.

Correspondence and requests for materials should be addressed to Ming-Sound Tsao or Housheng Hansen He.

Peer review information *Nature Genetics* thanks the anonymous reviewers for their contribution to the peer review of this work.

Reprints and permissions information is available at www.nature.com/reprints.

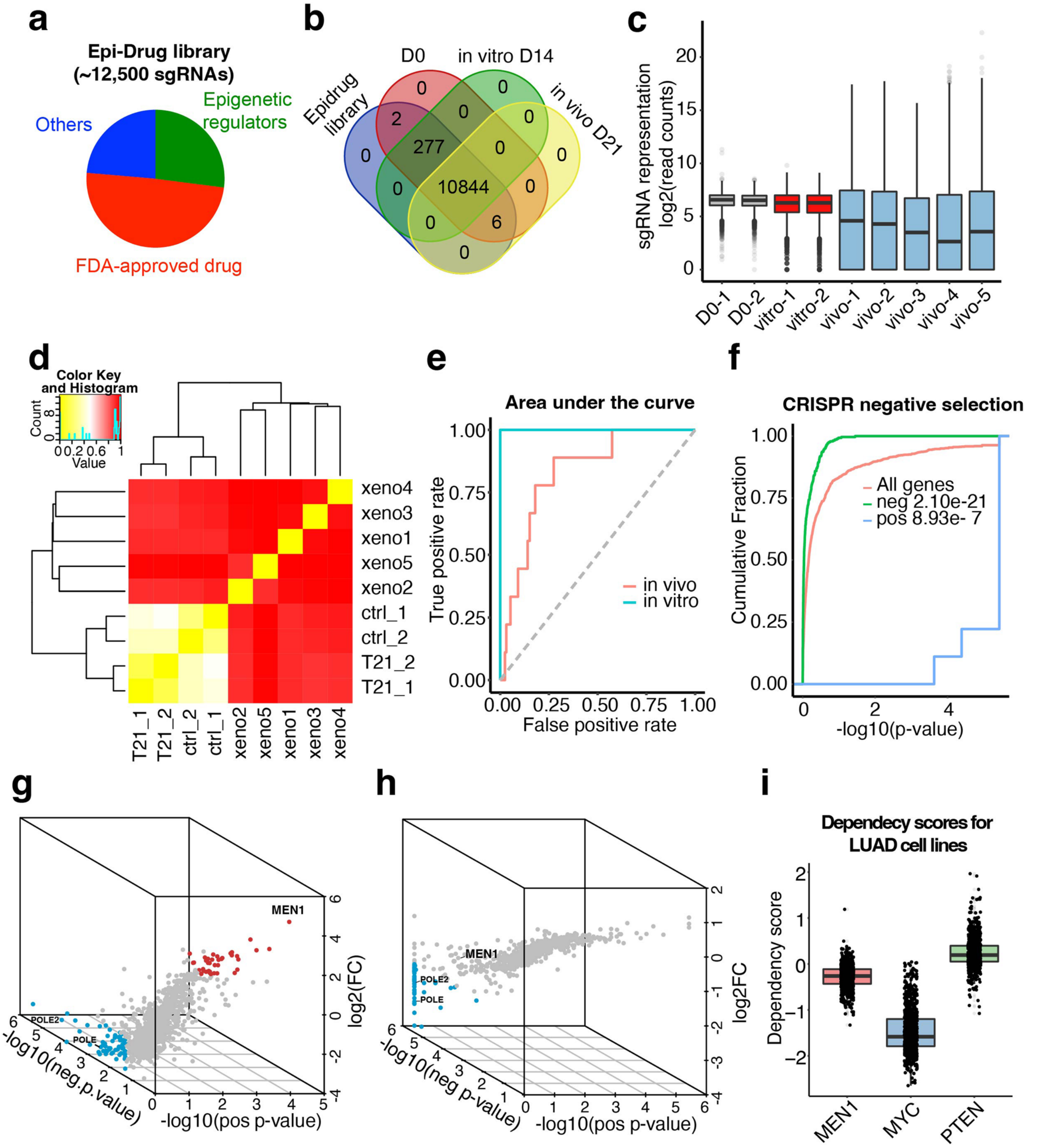

Extended Data Fig. 1 | CRISPR screening in A549 *in vivo* and *in vitro* using the EpiDrug library, Related to Fig. 1. **(a)** Composition of the EpiDrug sgRNA library. Pie chart illustrates the composition of the Epidrug sgRNA library that contains 12,472 sgRNAs targeting ~1,000 genes. **(b)** Number of sgRNAs detected in D0 and D21 screens. **(c)** Boxplot showing the distribution of log read counts of the complete 12.5k sgRNAs for D0 and D21 samples. Horizontal lines in the box represent the upper quartile, median, and the lower quartile from the top to the bottom. The vertical extending lines mark the 5th to 95th percentile. **(d)** Pairwise Pearson correlations of sgRNAs in D0 and D21 screens. **(e)** Receiver operating characteristic (ROC) curve of positive control genes in the screens. **(f)** Cumulative distribution of the -log10(p value) for negative selection of all Epi-Drug genes, positive and negative controls comparing D21 with D0 samples in the in vitro screens. p values (Wilcoxon test) are relative to Epi-drug candidate genes group (red line). **(g)** Dropout and enriched genes in D21 2D cultured cells compared to D0. The *p* values of positive and negative selections and log2(fold change) were defined and calculated by MAGeCK. **(h)** Dropout and enriched genes in D21 xenograft tumors compared to D0. The *p* values of positive and negative selections and log2(fold change) were defined and calculated by MAGeCK. **(i)** Dependency score of MEN1, MYC (oncogene) and PTEN (tumor suppressor) across 954 cancer cell lines of solid tumor types. Horizontal lines in the box represent the upper quartile, median, and the lower quartile from the top to the bottom.

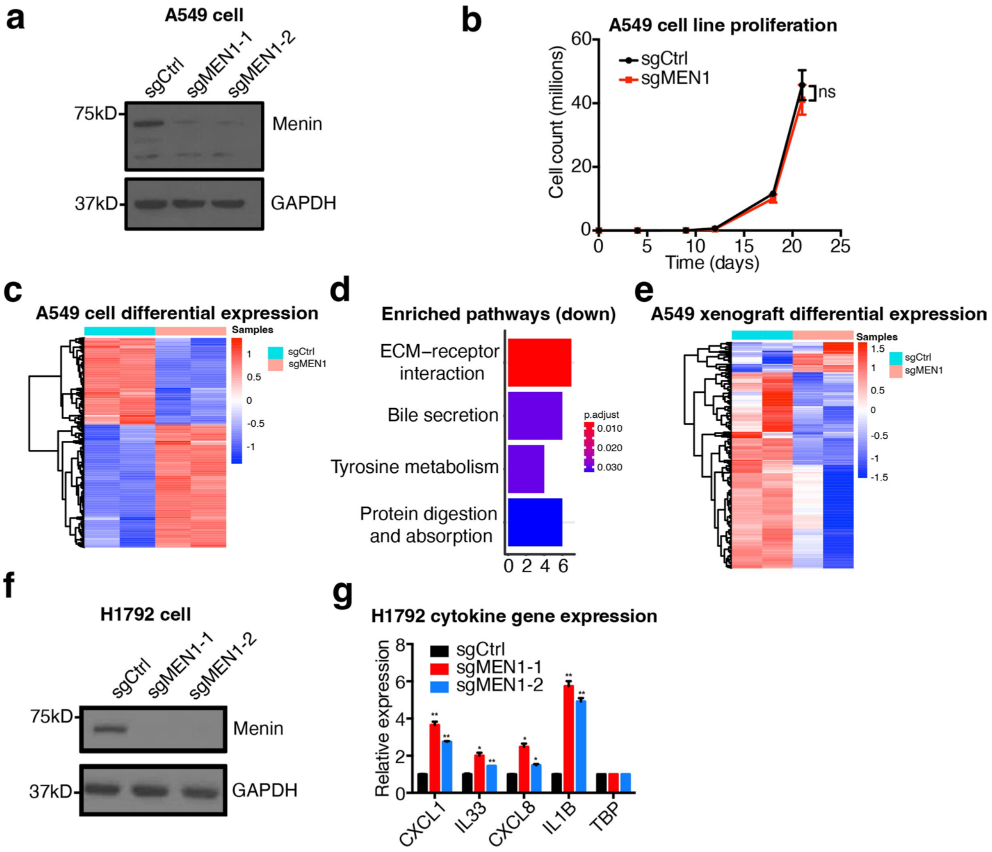

Extended Data Fig. 2 | MEN1 function in lung cancer cell line and xenograft models, related to Fig. 1. (a) Western Blot of MEN1 in control (sgCtrl) and MEN1 knockout (sgMEN1-1, sgMEN1-2) in A549 cells. GAPDH was used as loading control. **(b)** Cell proliferation rate of control and MEN1 knockouts A549 cells. Each data point represents mean ± s.e.m. cell counts (n=3 for each arm). Two-way ANOVA test was used for statistical analysis. **(c)** Heatmap showing differentially expressed genes in sgCtrl and MEN1 knockout A549 cells in 2D culture. **(d)** KEGG analysis of downregulated genes in 2D cultured MEN1 knockout A549 cells compared to the controls. X-axis represents the number of genes. Wald tests defined in DEseq2 were used to calculate the *p* values. **(e)** Heatmap showing differentially expressed genes in sgLacZ and MEN1 knockout A549 xenograft tumors. **(f)** Western Blot of control (sgCtrl) and MEN1 knockout (sgMEN1-1, sgMEN1-2) LUAD H1792 cells. GAPDH was used as a loading control. **(g)** RT-qPCR showing the relative expression of representative cytokine-related genes in MEN1 knockout H1792 cells compared to the controls. Data were normalized by the TBP gene. Mean ± s.e.m of 2 biological replicates were shown (unpaired two-tailed Student's t-test). *: *p* value <0.05; **: *p* value <0.01.

https://doi.org/10.1038/s41588-024-01874-9

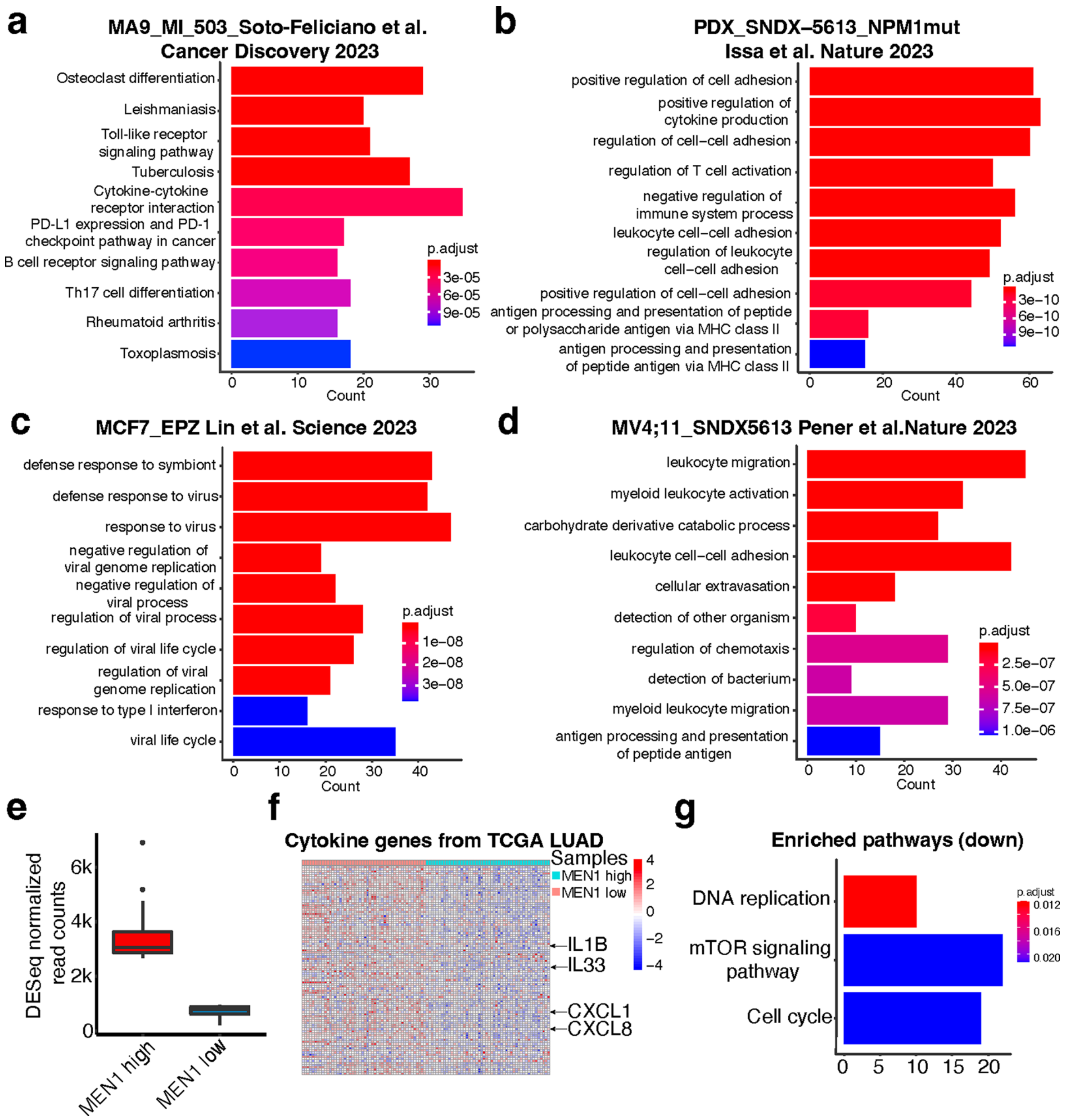

Extended Data Fig. 3 | MEN1 function in lung cancer public data, related to Fig. 1. **(a-d)** KEGG analysis of upregulated genes in MEN1 perturbed models compared to control using RNA-seq data from four recent publications. (Soto-Feliciano et al.[28] **(a)**; Issa et al.[26] **(b)**; Lin et al.[29] **(c)**; Pener et al. 2023. **(d)**). Gene signatures related to cytokine production and function were ranked at the top. Wald tests defined in DEseq2 were used to calculate the *p* values. **(e)** Boxplot shows relative abundance of MEN1 in the 20 MEN1-low and 20 MEN1-high patients from the TCGA LUAD cohort (wilcox, p-value = 1.451e-11). 20 patients with the highest and the lowest MEN1 expression were assigned to each group. Horizontal lines in the box represent the upper quartile, median, and the lower quartile from the top to the bottom. The vertical extending lines mark the 5th to 95th percentile. **(f)** Heatmap shows relative abundance of 100 genes in the KEGG term 'Cytokine-cytokine receptor interaction' in MEN1-low and MEN1-high patients from the TCGA LUAD cohort. **(g)** KEGG analysis of downregulated genes in MEN1-low compared to MEN1-high patients from the TCGA LUAD cohort. Wald tests defined in DEseq2 were used to calculate the *p* values.

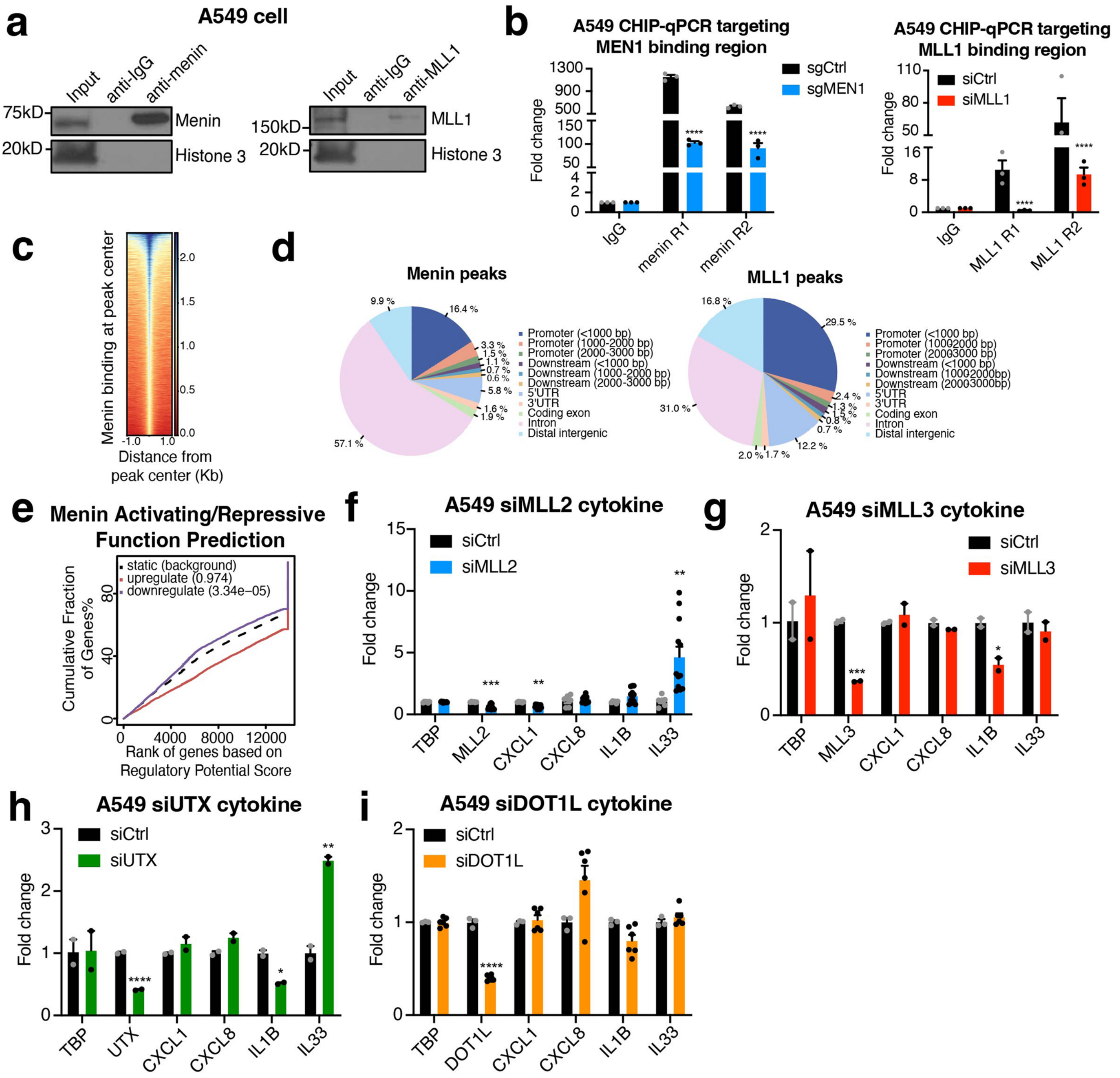

Extended Data Fig. 4 | Menin and MLL1 CUT&RUN analysis in A549 cells, related to Fig. 2. **(a)** Western blot of A549 lysate and immunoprecipitation product using IgG, menin (left), and MLL1 antibody (right). (**b**) ChIP-qPCR of representative MEN1 and MLL1 binding sites in A549 cells with and without MEN1 knockout. Mean ± s.e.m of 3 biological replicates were shown (unpaired two-tailed Student's t-test). ***: *p* value <0.001; ****: *p* value <0.0001. **(c)** Heatmap showing menin CUT&RUN binding intensity in A549 cells centered around MACS peak summit. (**d**) Genomic distribution of menin (left) and MLL1 (right) binding sites in A549 cells. **(e)** BETA regulation score for menin binding and differential genes in MEN1-low compared to MEN1-high patients from the TCGA LUAD cohort. (**f-h**) RT-qPCR showing the relative expression of representative cytokine-related genes in A549 cells with and without siRNA silencing of MLL2 (**f**), MLL3 (**g**), UTX (**h**) and DOT1L (**i**). Data were normalized by the TBP gene. Mean ± s.e.m of biological replicates were shown (unpaired two-tailed Student's t-test). *: *p* value <0.05; **: *p* value <0.01. Mean ± s.e.m of 2-12 biological replicates were shown (unpaired two-tailed Student's t-test).

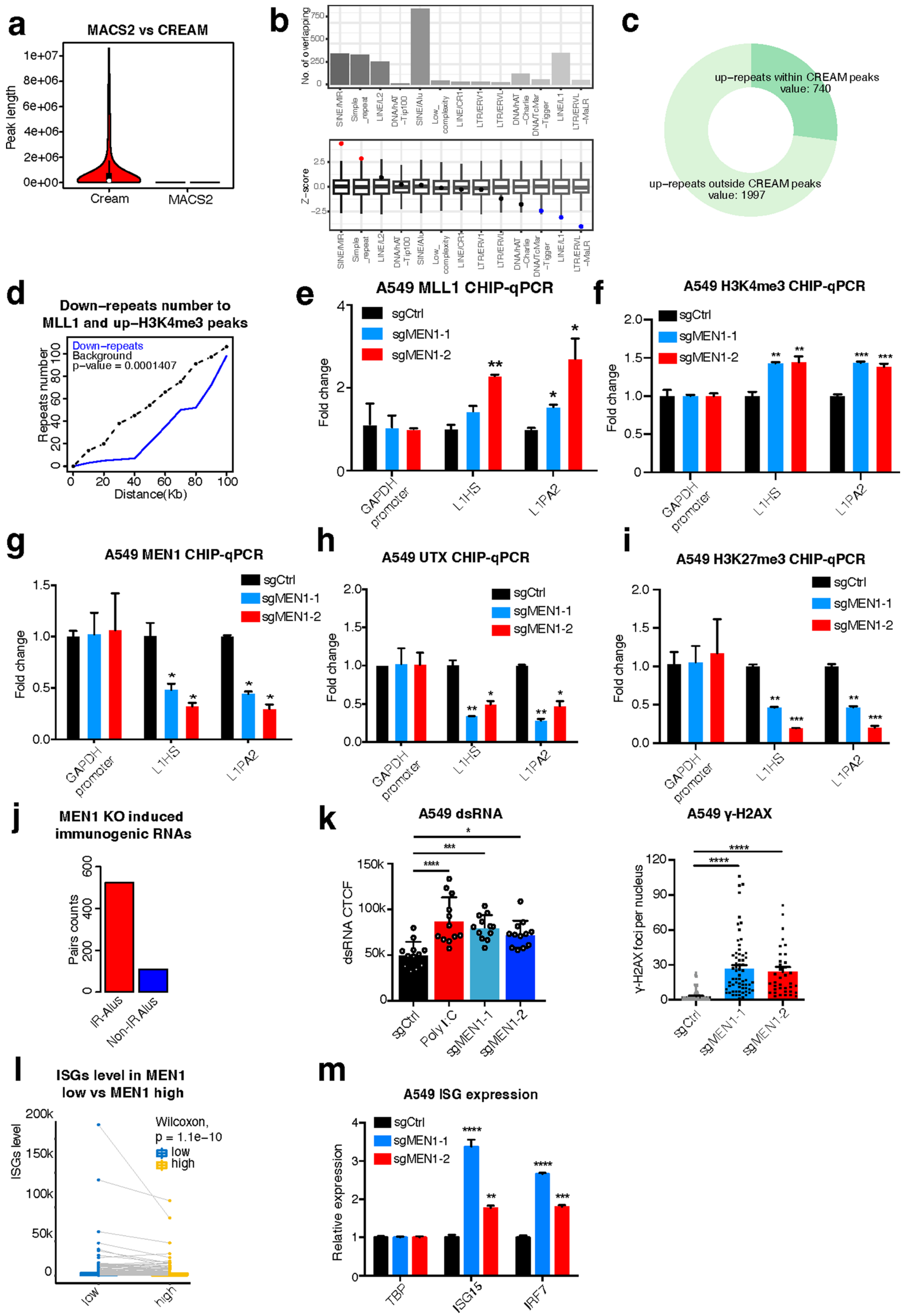

Extended Data Fig. 5 | See next page for caption.

Extended Data Fig. 5 | MEN1 perturbation caused repeat expression alteration in A549 cells, related to Fig. 2. (a) The distribution of peak length called by CREAM and MACS2 respectively. **(b)** Upper panel: Barplot showing the number of upregulated repeats in each subfamily. Lower panel: Boxplot showing permutation Z-score for upregulated repeats in each subfamily. Red color indicates statistical significance. Horizontal lines in the box represent the upper quartile, median, and the lower quartile from the top to the bottom. The vertical extending lines mark the 5th to 95th percentile. **(c)** Donut showing the number of upregulated repeats within and outside of the CREAM peak regions. (**d**) Number of downregulated repeats within a given distance of 1,857 peaks with increased H3K4me3 and MLL binding. Background are randomly selected repeat regions that do not show differential expression upon MEN1 knockout. p-value was calculated by one sided paired t-test. (**e-i**) ChIP-qPCR analysis of MLL1 **(e)**, H3K4me3 **(f)**, MEN1 **(g)**, UTX (**h**) and H3K27me3 (**i**) in A549 cells with and without knockout of MEN1. 3'UTR of LINE1-HS and LINE1-PA2 were selected for analysis. GAPDH promoter was used as control for normalization. Mean ± s.e.m of 2 biological replicates were shown (unpaired two-tailed Student's t-test). *: *p* value <0.05; **: *p* value <0.01; ***: *p* value <0.001. **(j)** Bar plot showing the number of inverted Alus and non-inverted Alus induced by MEN1 knockout. **(k)** Quantifications of immunofluorescence staining of dsRNA (left panel) and γ-H2AX (right panel). For dsRNA staining, Mean ± s.e.m of quantifications from 12 randomly picked fields were shown (unpaired two-tailed Student's t-test). *: *p* value < 0.05; **: *p* value < 0.01; ***: *p* value < 0.001. For γ-H2AX, Mean ± s.e.m of quantifications from 95, 67 and 42 randomly picked cells were shown for sgCtrl, sgMEN1-1, and sgMEN1-2 group respectively (unpaired two-tailed Student's t-test). ****: *p* value < 0.0001. **(l)** ISG gene expression levels in MEN1-low vs MEN1-high patient tumors in the TCGA LUAD cohort. **(m)** qRT-PCR showing the relative expression of representative ISGs in MEN1 knockout A549 cells relative to control cells. Housekeeping gene TBP was used as control.Mean ± s.e.m of 3 biological replicates were shown (unpaired two-tailed Student's t-test). ****: *p* value <0.0001.

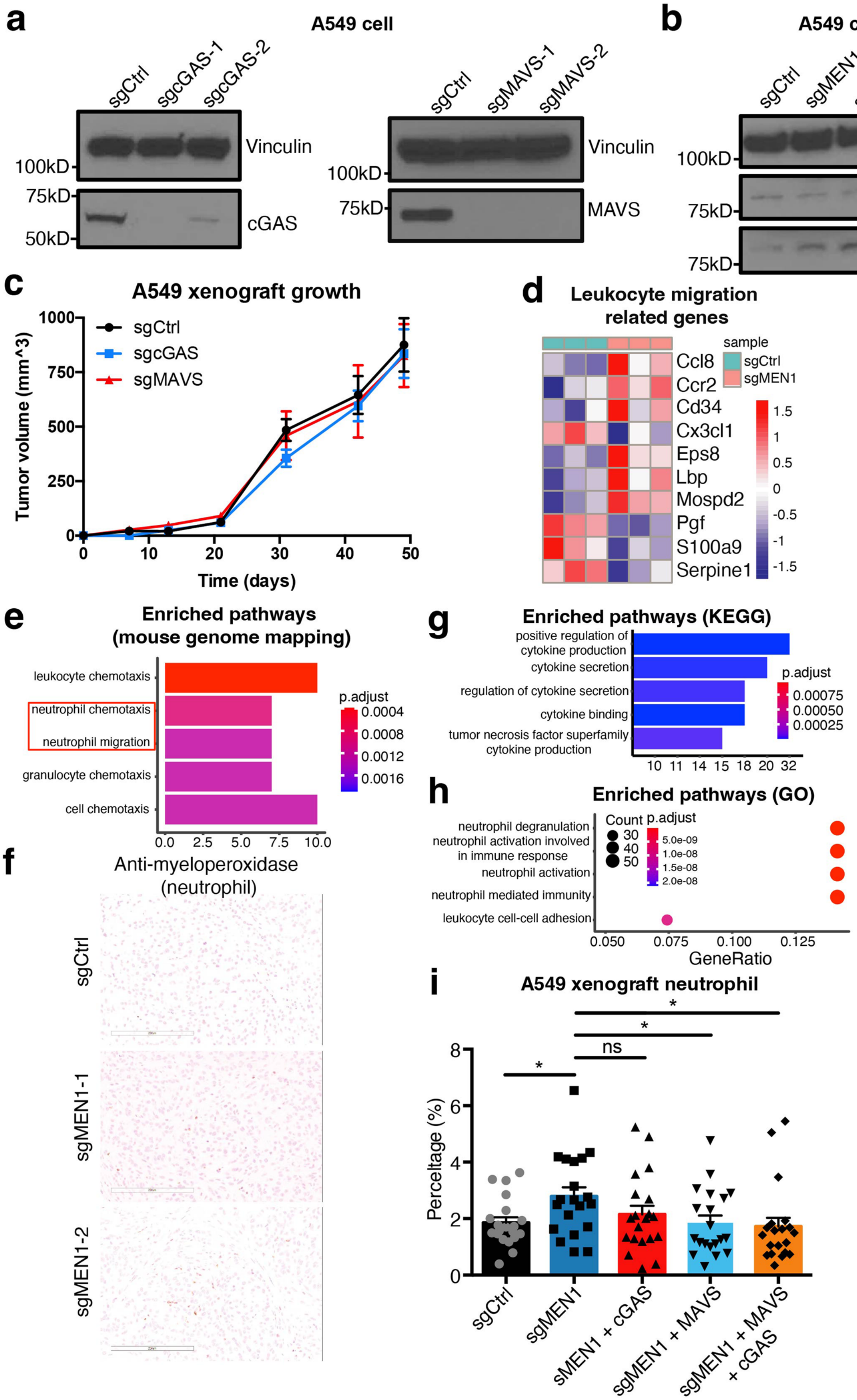

Extended Data Fig. 6 | See next page for caption.

Extended Data Fig. 6 | MEN1 and MLL1 regulation of cytokine-related genes expression and immune cell infiltration, related to Fig. 3. (a) Western blot showing control (sgCtrl), cGAS knockout (left; sgcGAS-1, sgcGAS-2) and MAVS knockout (right; sgMAVS-1, sgMAVS-2) A549 cells. Vinculin was used as a loading control. **(b)** Western blot of TBK1 and p-TBK1 in control (sgCtrl) and MEN1 knockout (sgMEN1-1, sgMEN1-2) A549 cells. Vinculin was used as a loading control. **(c)** Xenograft tumor growth curve in immunodeficient mice inoculated with control (sgCtrl), cGAS and MAVS knockout (sgcGAS, sgMAVS) A549 cells. Each data point represents mean ± s.e.m. tumor volumes (n=10 in sgCtrl, sgMEN1-1, and sgMEN1-2 group). Two-way ANOVA test was used for the statistical test of the growth curves. **(d)** Heatmap of upregulated genes ($p < 0.01$ and Log2(FC) > 1) in the leukocyte migration term in MEN1 knockout A549 xenograft tumors. **(e)** GO analysis of differentially expressed mouse genes in MEN1 knockout versus control A549 tumors. Neutrophil related terms are highlighted. Wald tests defined in DEseq2 were used to calculate the *p* values. **(f)** Representative IHC images showing the infiltration of neutrophils for control (sgCtrl) and MEN1 knockout (sgMEN1-1, sgMEN1-2) A549 xenograft tumors. **(g)** Bar plot showing enriched KEGG terms of 478 upregulated genes from menin inhibitor MI-389 treated MV4-11 human MLL leukemia cells. X-axis represents the number of genes. Wald tests defined in DEseq2 were used to calculate the *p* values. **(h)** Dot plot showing enriched GO terms of 478 upregulated genes from menin inhibitor MI-389 treated MV4-11 human MLL leukemia cells. Wald tests defined in DEseq2 were used to calculate the *p* values. **(i)** Percentage of infiltrated Neutrophil cells in A549 xenograft tumors with and without knockout of MEN1 or in combination with MAVS and/or cGAS knockout. Mean ± s.e.m of quantifications from 10 tumor IHC sections biological replicates were shown (unpaired two-tailed Student's t-test). *: *p* value <0.05.

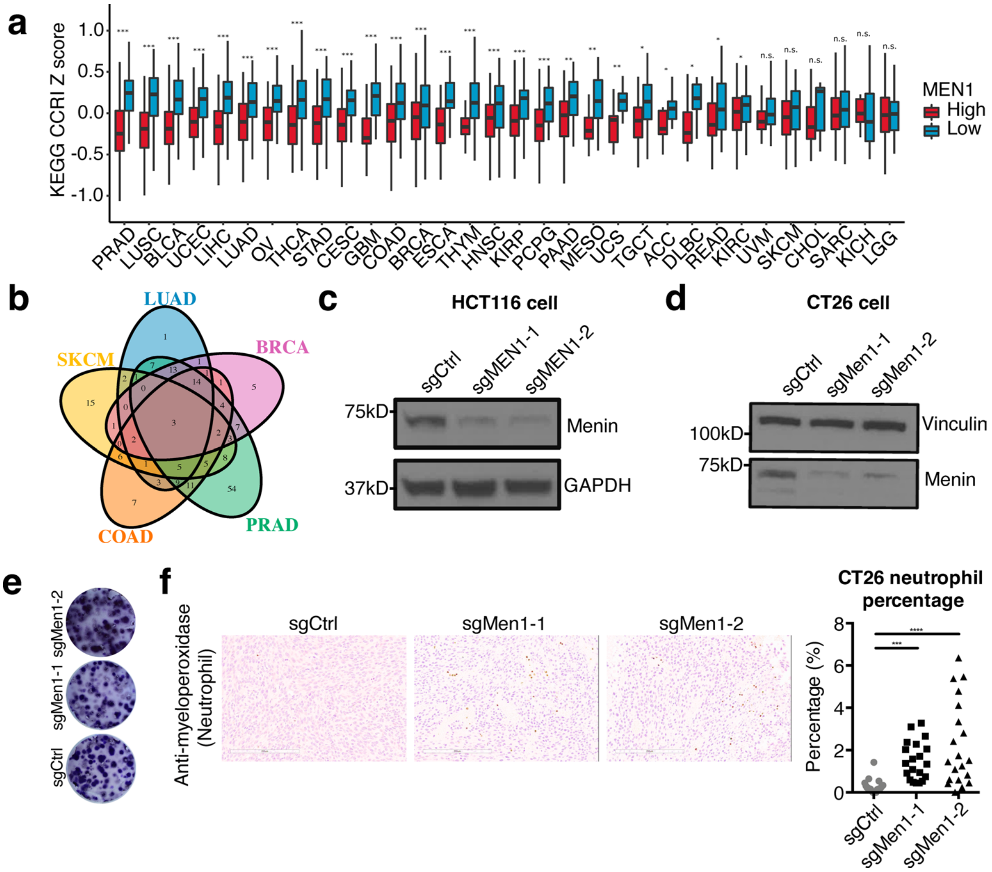

Extended Data Fig. 7 | Men1's function in immunodeficient models beyond lung cancer, related to Fig. 4. (**a**) Normalized cytokine-cytokine receptor interaction signature in MEN1-low and MEN1-high patients from 32 cancer (sub-)types from the TCGA cohorts. Mean ± s.d. of 8-224 biological replicates were shown (unpaired two-tailed Student's t-test). *: *p* value <0.05; **: *p* value <0.01; ***: *p* value <0.001. **(b)** Venn diagram showing overlap of cytokine-related genes upregulated in MEN1-low compared to MEN1-high patients of lung, colon, breast, prostate and skin cancer from the TCGA cohort. **(c)** Western blot of control (sgCtrl) and MEN1 knockout (sgMEN1-1, sgMEN1-2) HCT116 cells. GAPDH was used as a loading control. **(d)** Western blot of control (sgCtrl) and Men1 knockout (sgMen1-1, sgMen1-2) CT26 cells. Vinculin was used as a loading control. **(e)** Colony formation of CT26 cells with and without knockout of Men1. **(f)** Representative IHC images and dot plot summary showing the infiltration of neutrophils for control (sgCtrl) and Men1 knockout (sgMen1-1, sgMen1-2) CT26 tumors from immunodeficient mice. Quantifications from 10 tumor IHC sections were shown (unpaired two-tailed Student's t-test). ***: *p* value <0.001; ****: *p* value <0.0001.

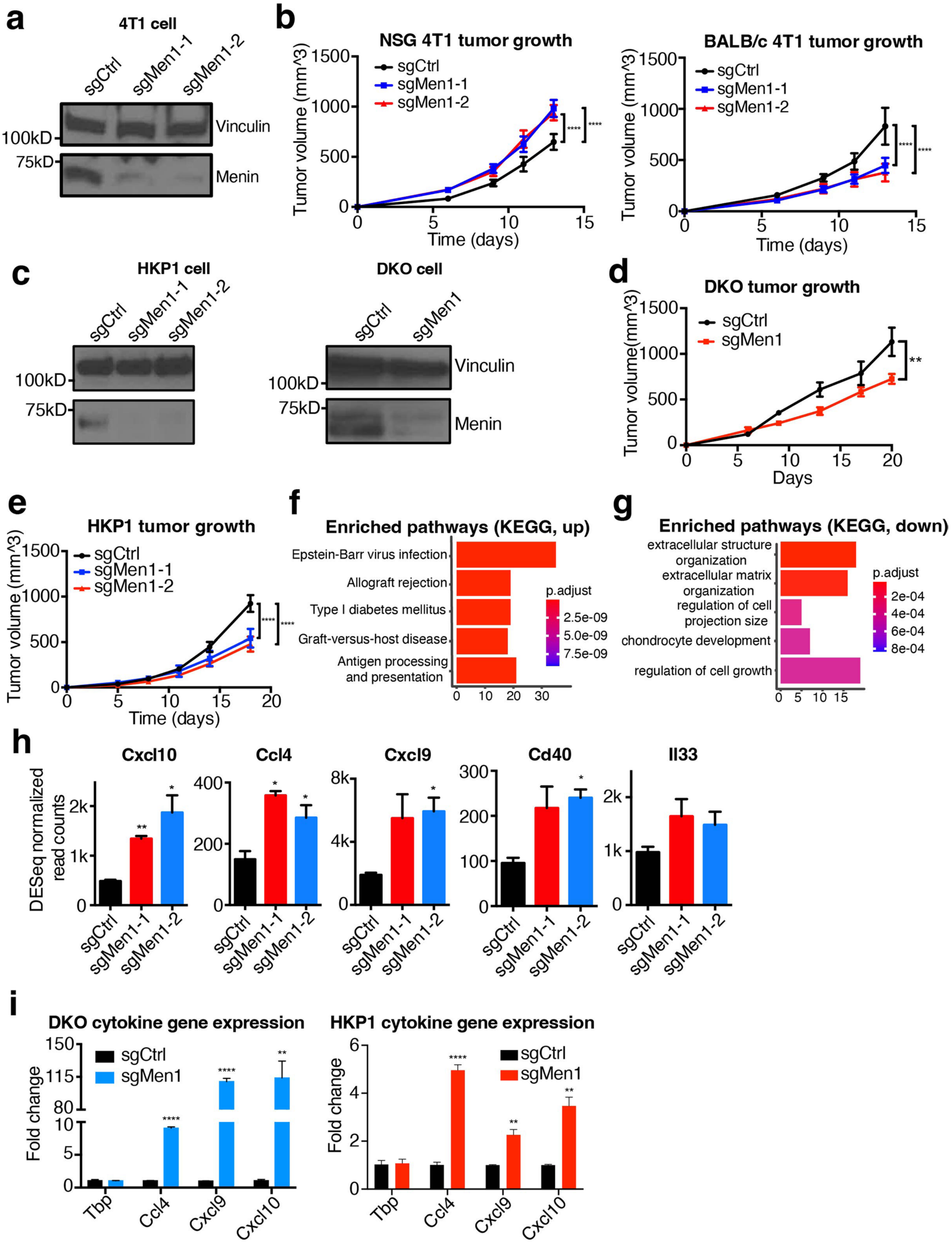

Extended Data Fig. 8 | See next page for caption.

Extended Data Fig. 8 | Men1's function in immunocompetent mouse models, related to Fig. 4. (a) Western blot analysis of Men1 in control (sgCtrl) and Men1 knockout (sgMen1-1, sgMen1-2) 4T1 mouse breast cancer cells. Vinculin was used as a loading control. **(b)** Tumor growth in immunodeficient (left) and immunocompetent (right) BALB/c mice inoculated with control (sgCtrl) or Men1 knockout (sgMen1-1, sgMen1-2) 4T1 cells. Each data point represents mean ± s.e.m. tumor volumes (n=10 in sgCtrl, sgMen1-1, and sgMen1-2 group). Two-way ANOVA test was used for the statistical test of the growth curves. ****: *p* value <0.0001. **(c)** Western blot analysis of Men1 in control (sgCtrl) and Men1 knockout (sgMen1-1, sgMen1-2) in HKP1 mouse lung cancer cells (left) and DKO mouse prostate cancer cells (right). Vinculin was used as a loading control. **(d)** Tumor growth in immunocompetent C57BL/6J mice inoculated with control (sgCtrl) or Men1 knockout (sgMen1-1, sgMen1-2) DKO cells. Each data point represents mean ± s.e.m. tumor volumes (n=7 in sgCtrl, and sgMen1 group). Two-way ANOVA test was used for the statistical test of the growth curves. **: *p* value <0.01 **(e)** Tumor growth in immunocompetent C57BL/6J mice inoculated with control (sgCtrl) or Men1 knockout (sgMen1-1, sgMen1-2) HKP1 cells. Each data point represents mean ± s.e.m. tumor volumes (n=10 in sgCtrl, sgMen1-1, and sgMen1-2 group). Two-way ANOVA test was used for the statistical test of the growth curves. ****: *p* value <0.0001. **(f)** KEGG analysis of up-regulated genes in Men1 KO versus control CT26 tumors was performed and top 5 terms were shown. X-axis represents the number of genes. Wald tests defined in DEseq2 were used to calculate the *p* values. **(g)** KEGG analysis of down-regulated genes in Men1 KO versus control CT26 tumors. Wald tests defined in DEseq2 were used to calculate the *p* values. **(h)** DESeq normalized read counts of Ccl4, Cxcl9 and Cxcl10 in control (sgCtrl) and Men1 knockout (sgMen1-1, sgMen1-2) CT26 tumors. Mean ± s.e.m of 2 or 3 biological replicates were shown (unpaired two-tailed Student's t-test). *: *p* value <0.05; **: *p* value <0.01 **(i)** RT-qPCR showing the abundance of representative cytokine-related genes in Men1 knockout DKO cells (left) and HKP1 cells (right) compared to the control cells. Mean ± s.e.m of 3 biological replicates were shown (unpaired two-tailed Student's t-test). **: *p* value <0.01; ****: *p* value <0.0001.

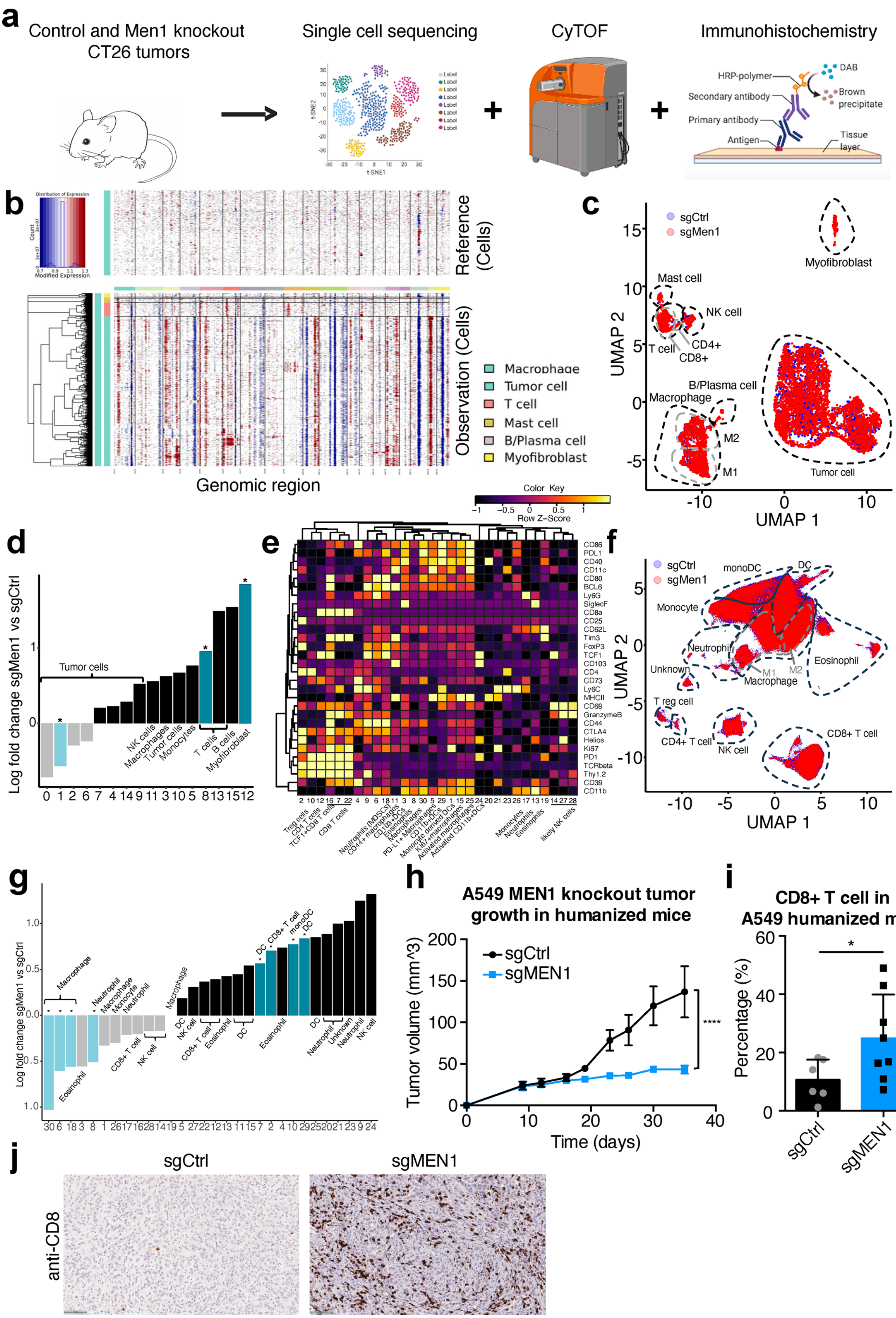

Extended Data Fig. 9 | See next page for caption.

Extended Data Fig. 9 | scRNA-seq and CyTOF analysis reveal increased immune cell infiltration in Men1 knockout CT26 tumors, related to Fig. 6. (a) Schematic view of CT26 tumor scRNA-seq and CyTOF experiments. **(b)** Inferred copy number (CNA) for all the cells. Red indicates copy number gain and blue indicates copy number loss. **(c)** UMAP view of single cells from scRNA-seq profiling, color coded by tumor samples with (red) or without (blue) deletion of Men1. (**d**) Bar plot showing the differences of the number of cells in each sub-clusters in Men1-knockout versus control tumor samples from scRNA-seq profiling. (**e**) Heatmap showing the marker gene expression in each sub-clusters. (**f**) UMAP view of single cells from CyTOF profiling, color coded by tumor samples with (red) or without (blue) deletion of Men1. (**g**) Bar plot showing the differences of the number of cells in each sub-clusters in Men1-knockout versus control tumor samples from CyTOF profiling. **(h)** Tumor growth rate of A549 xenograft in humanized mice with and without knockout of MEN1. Each data point represents mean ± s.e.m. tumor volumes (n = 5 in sgCtrl and sgMEN1 group). Two-way ANOVA test was used for the statistical test of the growth curves. ****: *p* value <0.0001. **(i)** Bar plot showing the percentage of infiltrated CD8+ T cells in tumors with and without knockout of MEN1. Mean ± s.d. of quantifications from 6 and 8 IHC sections for sgCtrl and sgMEN1biological replicates were shown for each measurement (unpaired two-tailed Student's t-test). *: *p* value <0.05. **(j)** Representative images of CD8+ T cell staining in tumors with and without knockout of MEN1.

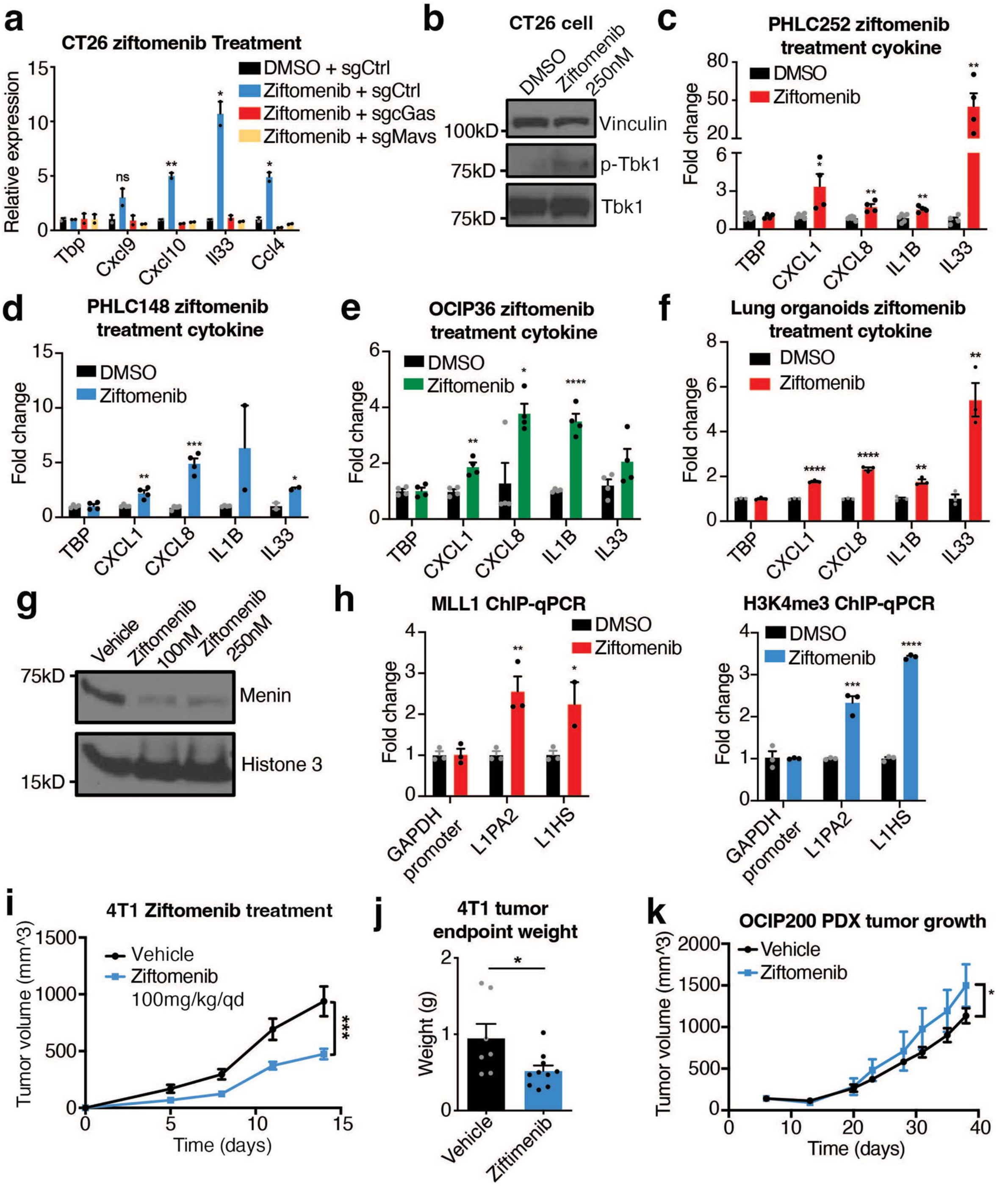

Extended Data Fig. 10 | Pharmacological inhibition of menin reduces tumor growth in syngeneic models in a similar mechanism, related to Fig. 6. (**a**) qRT-PCR showing the abundance of representative cytokine-related genes with ziftomenib treatment or in combination with cGas or Mavs knockout in CT26 cells. Housekeeping gene Tbp was used as a control. Mean ± s.e.m. of 2 biological replicates were shown for each measurement (unpaired two-tailed Student's t-test). *: *p* value <0.05; **: *p* value <0.01. (**b**) Western blot of total and phospho-TBK1 in DMSO (Ctrl) and ziftomenib treated CT26 mouse colon cancer cells. Vinculin was used as a loading control. (**c-e**) RT-qPCR showing the expression of representative cytokine-related genes in lung and pancreatic cancer explant PDX tissues with DMSO (Ctrl) or ziftomenib treatment. Mean ± s.e.m. of 2-4 biological replicates were shown for each measurement (unpaired two-tailed Student's t-test). ***: *p* value <0.001; ****: *p* value <0.0001. (**f**) RT-qPCR showing the expression of representative cytokine-related genes in a lung cancer patient-derived organoid model with DMSO (Ctrl) or ziftomenib treatment. Mean ± s.e.m. of 3 biological replicates were shown for each measurement (unpaired two-tailed Student's t-test). **: *p* value <0.01; ****: *p* value <0.0001. (**g**) Western blot of menin in DMSO or ziftomenib treated A549 cells. (**h**) ChIP-qPCR results showing increased binding of MLL1 and H3K4me3 at selective repeat regions in A549 cells with ziftomenib treatment. Mean ± s.e.m. of 3 biological replicates were shown for each measurement (unpaired two-tailed Student's t-test). *: *p* value <0.05; ***: *p* value <0.001; ****: *p* value <0.0001. (**i**) 4T1 tumor growth with vehicle or ziftomenib treatment. Each data point represents mean ± s.e.m. tumor volumes (n=10 for each arm). Two-way ANOVA test was used for statistical analysis. ***: *p* value < 0.001. (**j**) Harvested 4T1 tumor weight from the mice treatment with vehicle or ziftomenib at the experimental endpoint. Mean ± s.e.m. of 7 and 10 biological replicates for vehicle and ziftomenib treatment group were shown for each measurement (unpaired two-tailed Student's t-test). *: *p* value <0.05 (**k**) Tumor growth of pancreatic PDX model OCIP200 in immunodeficient NOD-SCID mice treated with DMSO or ziftomenib. Each data point represents mean ± s.e.m. tumor volumes (n=5 for each arm). Two-way ANOVA test was used for statistical analysis. *: *p* value <0.05. **a**, Created with BioRender.com.

nature research

Corresponding author(s): Housheng Hansen He
Ming-Sound Tsao

Last updated by author(s): 2024/06/25

Reporting Summary

Nature Research wishes to improve the reproducibility of the work that we publish. This form provides structure for consistency and transparency in reporting. For further information on Nature Research policies, see our Editorial Policies and the Editorial Policy Checklist.

Statistics

For all statistical analyses, confirm that the following items are present in the figure legend, table legend, main text, or Methods section.

n/a	Confirmed	
☐	☒	The exact sample size (*n*) for each experimental group/condition, given as a discrete number and unit of measurement
☐	☒	A statement on whether measurements were taken from distinct samples or whether the same sample was measured repeatedly
☐	☒	The statistical test(s) used AND whether they are one- or two-sided *Only common tests should be described solely by name; describe more complex techniques in the Methods section.*
☐	☒	A description of all covariates tested
☐	☒	A description of any assumptions or corrections, such as tests of normality and adjustment for multiple comparisons
☐	☒	A full description of the statistical parameters including central tendency (e.g. means) or other basic estimates (e.g. regression coefficient) AND variation (e.g. standard deviation) or associated estimates of uncertainty (e.g. confidence intervals)
☐	☒	For null hypothesis testing, the test statistic (e.g. *F*, *t*, *r*) with confidence intervals, effect sizes, degrees of freedom and *P* value noted *Give P values as exact values whenever suitable.*
☒	☐	For Bayesian analysis, information on the choice of priors and Markov chain Monte Carlo settings
☒	☐	For hierarchical and complex designs, identification of the appropriate level for tests and full reporting of outcomes
☐	☒	Estimates of effect sizes (e.g. Cohen's *d*, Pearson's *r*), indicating how they were calculated

Our web collection on statistics for biologists contains articles on many of the points above.

Software and code

Policy information about availability of computer code

Data collection	Confocal images were acquired using Zeiss LSM700 Confocal microscope, Zeiss Zen software and FIJI ImageJ. qPCRs were run on Bio-Rad CFX Real-Time System. The Western blots were exposed on Thermo Scientific CL-XPosure film.
Data analysis	All data analysis details, including method and detailed parameters are described in Methods. Customized code for data analyzing and plotting has been deposited at Github (https://github.com/liuyin111/MEN1-in-regulating-tumor-microenvironment-interactions). Software used: R statistical environment (v3.4.1);STAR (v2.4.2a);HTSeq (v0.6.1);fastqc (v0.11.5);RSeQC (2.6.4); MaxQuant (version 1.5.2.8). R packages:DESeq2 (v1.22.2); GenomicFeatures (v1.28.5); ConsensusClusterPlus (v1.38.0); Guitar (v1.20.1); clusterProfiler (v3.10.1); Bowtie (v.1.1.2); MAGeCK (v0.5.4); survminer(0.4.6); BPG (v5.9.8); ggplot2 (3.1.0). Website: g:Profiler (v0.6.4); FlowJo V10, CyTOF software version 6.7 and Cytobank6.2 (Cytobank, Inc).

For manuscripts utilizing custom algorithms or software that are central to the research but not yet described in published literature, software must be made available to editors and reviewers. We strongly encourage code deposition in a community repository (e.g. GitHub). See the Nature Research guidelines for submitting code & software for further information.

Data

Policy information about availability of data

All manuscripts must include a data availability statement. This statement should provide the following information, where applicable:

- Accession codes, unique identifiers, or web links for publicly available datasets
- A list of figures that have associated raw data
- A description of any restrictions on data availability

All sequencing data and rocessed data are deposited in the Gene Expression Omnibus (GEO) under the accession GSE194355 and GSE197595. Public data that are analyzed in the study were obtained from GEO and the accession numbers are available in the respective method sections.

Field-specific reporting

Please select the one below that is the best fit for your research. If you are not sure, read the appropriate sections before making your selection.

☒ Life sciences ☐ Behavioural & social sciences ☐ Ecological, evolutionary & environmental sciences

For a reference copy of the document with all sections, see nature.com/documents/nr-reporting-summary-flat.pdf

Life sciences study design

All studies must disclose on these points even when the disclosure is negative.

Sample size	Sample sizes were not predetermine by any statistical methods. Generally, sample size was based on our prior experience and common standards in the field for detecting statistically significant differences between conditions, and also based on experimental feasibility, sample availability, and necessary to obtain definitive results.
Data exclusions	All data were used without exclusions.
Replication	CRISPR screen were done using at least two replicates for each time point. RNA-seq were performed with the sample size of two for each cell line at each condition. RT-qPCR were performed with biological replicates. 5-10 mice were used for each treatment arms.
Randomization	Randomization not deemed essential for experiments using cell lines, since they are divided and expanded from a relatively homogeneous cell population. For inhibitor treatment experiments using PDX and xenograft models, the mice were assigned to vehicle or treatment group(s) to minimize the difference between the average tumor sizes between these groups before initial treatment.
Blinding	Blinding was not possible to our study, because of the time constraint and the limitation of the human resource for animal work.

Reporting for specific materials, systems and methods

We require information from authors about some types of materials, experimental systems and methods used in many studies. Here, indicate whether each material, system or method listed is relevant to your study. If you are not sure if a list item applies to your research, read the appropriate section before selecting a response.

Materials & experimental systems

n/a	Involved in the study
☐	☒ Antibodies
☐	☒ Eukaryotic cell lines
☒	☐ Palaeontology and archaeology
☐	☒ Animals and other organisms
☒	☐ Human research participants
☒	☐ Clinical data
☒	☐ Dual use research of concern

Methods

n/a	Involved in the study
☐	☒ ChIP-seq
☐	☒ Flow cytometry
☒	☐ MRI-based neuroimaging

Antibodies

Antibodies used	menin antibody (Bethyl laboratories, A300-115A), KMT2A/MLL1 antibody (Abcam, ab272023), H4K4me3 antibody (ab8580, Abcam), J2 monoclonal antibody (Mouse anti double-stranded RNA, Nordic MUbio, 10010500), cGAS antibody (Cell Signaling Technology, 15102S), MAVS antibody (Santa Cruz Biotechnology, sc-365333), Anti-Myeloperoxidase antibody (Abcam, ab9535), H3K27me3 antibody (ab6002, Abcam), UTX antibody (A302-374A, Bethyl Laboratories), and Anti-mouse IgG (H+I) F(ab')2 Fragment-Alexa Fluor 647 Conjugate (Cell Signaling Technology, 4410S).
Validation	Validation statements and literature citations of each antibody can be found on the manufacturer's website and/or the CiteAb website:

anti-Menin (https://www.thermofisher.com/antibody/product/Menin-Antibody-Polyclonal/A300-105A)
anti-MLL1 (https://www.abcam.com/kmt2a--mll-antibody-ab272023.html)
anti-H3K4me3 (https://www.abcam.com/en-ca/products/primary-antibodies/histone-h3-tri-methyl-k4-antibody-chip-grade-ab8580)
anti-J2 monoclonal (http://www.nordicmubio.com/products/mouse-anti-double-stranded-rna-j2/10010500)
anti-cGAS (https://www.cellsignal.com/products/primary-antibodies/cgas-d1d3g-rabbit-mab/15102)
anti-MAVS (https://www.scbt.com/p/mavs-antibody-c-1)
anti-Myeloperoxidase (https://www.abcam.com/myeloperoxidase-antibody-ab9535.html)
anti-H3K27me3 (https://www.abcam.com/en-ca/products/primary-antibodies/histone-h3-tri-methyl-k27-antibody-mabcam-6002-chip-grade-ab6002)
anti-UTX (https://www.thermofisher.com/antibody/product/UTX-Antibody-Polyclonal/A302-374A)

Eukaryotic cell lines

Policy information about cell lines

Cell line source(s)	A549 (Cat. #CCL-185), H1792 (Cat. #CRL-5895), HCT116 (Cat. #CCL-247), 4T1 (Cat. #CRL-2539) and CT26 (Cat. #CRL-2638) were purchased from the American Type Culture Collection (ATCC).
Authentication	A549, H1792, HCT116, 4T1 and CT26 cells have been authenticated by STR analysis, as declared by ATCC.
Mycoplasma contamination	A549, H1792, HCT116, 4T1 and CT26 cells have been tested negative for Mycoplasma contamination by the MycoAlert Mycoplasma Detection Kit (Cat. #LT07-118, Lonza).
Commonly misidentified lines (See ICLAC register)	No

Animals and other organisms

Policy information about studies involving animals; ARRIVE guidelines recommended for reporting animal research

Laboratory animals	Six-week old NOD/SCID, C57BL6 and BALB/c mice were obtained from Princess Margaret Cancer Centre Animal Research Centre. The mice were housed under standard temperature at 21C-22C, humidity at 45%-60%, and timed lighting conditions at 12hr/12hr light/dark cycle mandated by the committee.
Wild animals	No wild animals were used in this study.
Field-collected samples	No field collected samples were used in the study.
Ethics oversight	All procedures were performed in accordance with the International Guidelines for the Use of Animals and approved by the Animal Care Committee at UHN.

Note that full information on the approval of the study protocol must also be provided in the manuscript.

ChIP-seq

Data deposition

☒ Confirm that both raw and final processed data have been deposited in a public database such as GEO.

☒ Confirm that you have deposited or provided access to graph files (e.g. BED files) for the called peaks.

Data access links *May remain private before publication.*	https://www.ncbi.nlm.nih.gov/geo/query/acc.cgi?acc=GSE194355
Files in database submission	sgCtrl_MEN1_rep1 sgCtrl_MEN1_rep2 sgCtrl_MLL1_rep1 sgCtrl_MLL1_rep2 sgCtrl_H3K4me3_rep1 sgCtrl_H3K4me3_rep2 sgMEN1_1_MLL_rep1 sgMEN1_1_MLL_rep2 sgMEN1_2_MLL_rep1 sgMEN1_2_MLL_rep2
Genome browser session (e.g. UCSC)	Not available

Methodology

Replicates	2
Sequencing depth	70M, 75bp length, pair-end
Antibodies	A300-115A, ab272023, ab8580
Peak calling parameters	MACS with default parameters
Data quality	The ChIP-seq data were visualized in IGV. A total of 26,507 and 10,521 peaks were identified over q-value of 0.05 for MEN1 and MLL1 in wild type A549 cells.
Software	Bowtie2 and MACS

Flow Cytometry

Plots

Confirm that:

☒ The axis labels state the marker and fluorochrome used (e.g. CD4-FITC).

☒ The axis scales are clearly visible. Include numbers along axes only for bottom left plot of group (a 'group' is an analysis of identical markers).

☒ All plots are contour plots with outliers or pseudocolor plots.

☒ A numerical value for number of cells or percentage (with statistics) is provided.

Methodology

Sample preparation	Single cell suspensions from individual samples were washed with PBS and pulsed with 12.5µM Cisplatin (Fluidigm) in PBS for 1 min prior to quenching with CyTOF staining media [Mg+/Ca+ HBSS containing 2% FBS (Multicell), 10mM HEPES (Corning), and FBS underlay]. Cells were then fixed for 12 min at room temperature with transcription factor fixative (Bioscience, 00-5523-00), permeabilized and individual samples barcoded according to manufacturer's instructions (Fluidigm 20-Plex Pd Barcoding Kit, 201060), prior to being combined. Combined samples were resuspended in staining media containing metal-tagged surface antibodies and Fc block (CD16/32; Bioxcell) for 30 minutes at 4°C. Cells were washed, then permeabilized and stained with metal tagged intracellular antibodies using Transcription Factor Staining Buffer Set. Cells were incubated in PBS containing 0.3% (w/v) saponin (Sigma, S7900-25G), 1.6% (v/v) paraformaldehyde (Polysciences Inc) and 50nM Iridium (Fluidigm) for one hour at room temperature.
Instrument	Helios2 mass cytometer (Fluidigm).
Software	FlowJo V10, CyTOF software version 6.7 and Cytobank6.2 (Cytobank, Inc).
Cell population abundance	Cells collected for following experiments CD45 positive via flow cytometor sorting.
Gating strategy	CD45 was used to enrich for immune cells.

☒ Tick this box to confirm that a figure exemplifying the gating strategy is provided in the Supplementary Information.